ROMANIAN ACADEMY

Institute of Physical Chemistry "Ilie Murgulescu"

Abstract of doctoral thesis

Molecular and Supramolecular Systems Evidencing Spin Interactions

Scientific supervisor:

Dr. Ioniță Elena Gabriela

PhD Student:

Buta Maria-Cristina

Bucharest

2020

The complete content of the thesis

Keywords

Electronic paramagnetic resonance, density functional theory, molecular modeling, structure-properties correlations, spin coupling, hyperfine interaction, dipolar coupling, organic biradicals, host-guest supramolecular systems.

Foreword

This work is dedicated to the exploration of new details and correlations concerning spins chemistry of various systems and phenomena: the interaction with the external field (relevant for the electronic paramagnetic resonance- EPR, or magnetic susceptibility measurements), the spin-spin effects (exchange or dipolar couplings) or the interaction with magnetic nuclei (hyperfine coupling). The case studies are collected from different chemical classes, such as stable organic radicals based on nitroxide groups, unstable organic radicals resulted from polyaromatic systems, mononuclear and polynuclear coordination compounds. The experimental parts, mostly related with the applications of the EPR techniques, are complemented with systematic modeling studies, aiming the rationalization of the measured properties by means of structural considerations. In this view, several numeric experiments were conceived, in order to answer to dedicated questions, the outcome resulting in new methodological advances and magneto-structural correlations.

The shortened thesis report follows the structure of the full text, including the section names, though in a different labelling of the corresponding entries.

Acknowledgements

This work was supported by the allowance provided within the Advanced Study Program of Romanian Academy (contract SCOSAAR 49/2016), having also the support of the UEFISCDI-PCE 108/2017 research grant.

Warm thanks to the scientific adviser, dr. Gabriela Ioniţă, who gave me full support in the realization of this work, showing a broad opening to cooperation, offering me to possibility extend my previous scientific interests, continuing the studies on coordination compounds, being indebted in this part to dr. Marilena Ferbinteanu and benefitting from the support of dr. Fanica Cimpoesu and dr. Ana-Maria Toader, from the group of theoretical chemistry.

I am grateful to my family and close friends for support along the realization of this thesis. I dedicate this work to the memory of my father.

Maria Cristina Buta

Chapter I

The chemistry of spin interactions

I.a. The electronic spin and molecular magnetism. The spin coupling. The effective Hamiltonians. The Interaction in magnetic Field. The Electronic Paramagnetic Resonance Spectroscopy (EPR)

The first chapter is dedicated to introductory issues, regarding approached classes of compounds, instrumental techniques and principles of molecular modeling and magneto-structural correlations.

The electronic spin is a fundamental component of the quantum nature of matter, determining the chemical bond itself and intervening in all the magnetic properties of molecules and materials [1]. The work has as red line the idea of spin interactions, met in various systems and circumstances, focusing on their correlation with the structure of molecular and supramolecular edifices, exploring the underlying mechanisms.

Aside the well-established use of instrumental techniques based on the electronic spin, such as the electronic paramagnetic resonance (EPR) [2,3], on the background of the modern paradigms of the molecular magnetism [4,5], there are great expectations about the futuristic domain of the „spintronics" [6], yet in the stage of speculation and desiderata.

This chapter deals with selected introductory aspects, from generalities about phenomenological spin Hamiltonian to certain details concerning the molecular modeling techniques.

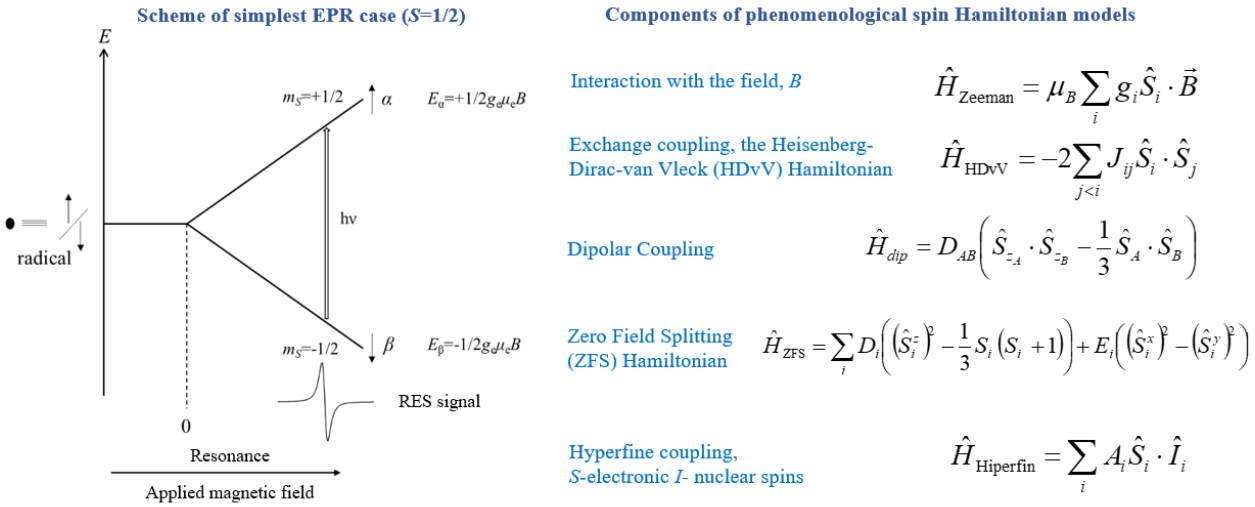

Figure I.1. Synopsis of the EPR spectroscopy (left side) and the overview of spin Hamiltonian parametric models encountered in EPR and other magnetic measurements.

The Figure I.1 shows the simplest case of an EPR experiment (for S=1/2, i.e. one unpaired electron) and offers a briefing over the spin interaction types encountered in molecular magnetism measurements and modeling. The EPR is based on the field-induced separation between the S_z projections belonging to the S spin quantum number, which in the absence of the field may have the $2S$+1 degeneracy. The EPR sample undergoes, aside the applied field, a radiofrequency (most frequently at about 9.8 GHz, the so-called X-band), the resonances (transitions) occurring when the gap between states equals its energy. In this way, the EPR works at a very small energy scale (fractions of reciprocal centimetres, cm^{-1}), being sensitive to subtle structural details. On this fact is based the spin-probe utility of properly conducted and interpreted EPR procedures, the spin carriers acting as "spies", providing structural information from complex media (solutions, gels, life systems) [7-9].

The right side of Figure I.1 enlists the generic expressions (as parametric Hamiltonians) of the interactions intervening and accounted in EPR techniques. The most important is the Zeeman interaction with the external field, introducing the gyromagnetic Landé factors, g (possibly dichotomized in projections on the Cartesian axes) characterizing a given paramagnetic centre. The paramagnetic sites may be involved in mutual interactions, either in the form of exchange coupling, i.e. a phenomenon of pure quantum nature (described by the so-called Heisenberg-Dirac-van Vleck Hamiltonian, labelled HDvV), or in the dipolar form, which emerges from the classical effects between oriented magnetic moments.

The dipolar interaction is projected in the quantum form as a Zero-Field- Splitting (ZFS) effect, which, as etymology makes quite explicit, represents a removal of the $2S$+1 degeneracy of a spin multiplet (only if $S\geq1$) even in the absence of magnetic field. In the case of dipolar-based ZFS, the referred S state is a collective one, e.g. the triplet resulted from the spin algebra of two unpaired electrons with individual S_1=S_2=1/2. In the case of metal ions, there is another source of ZFS effects, namely the spin-orbit coupling, which act on both localized spins of the paramagnets and on their collective, coupled, states. Another important element on the panoply of spin Hamiltonians is the interaction between electronic and nuclear spins, called hyperfine coupling. We will debate each type of the above-mentioned interactions and spin Hamiltonian parameters, in the course of case studies proposed in this work.

I.b. Selected Examples of Spin Coupled Systems. Stable Organic Radicals. Modeling and computational methods. Case study on the experiment-modeling complementarity

One of the most intensely EPR- studied class of compounds consists in radicals based on the nitroxide group, which, usually embedded in saturated carbon cycles form stable organic compounds. The nitroxide-based radicals show a large variety of manifestations, displaying ferromagnetic [10] or antiferromagnetic [11] couplings, magnetic phase transitions [12], with mechanisms driven by supramolecular effects [13,14]. The molecule abbreviated as TEMPO ((2,2,6,6-Tetramethylpiperidin-1-yl) oxyl), functionalized in various ways, is one of the preferred spin carriers for deals concerning spin label techniques and related modeling.

The Figure I.2 shows the orbital scheme responsible for the unpaired electron in the TEMPO molecule. Namely, the spin is lodged in the antibonding π^* -type molecular orbital (MO) of the N-O group (this being the Single Occupied Molecular Orbital-SOMO), while the π-bonding congener is doubly occupied. From the isosurfaces represented in the (c) panel, one may infer that the spin density is distributed approximately comparable on the nitrogen and oxygen atoms.

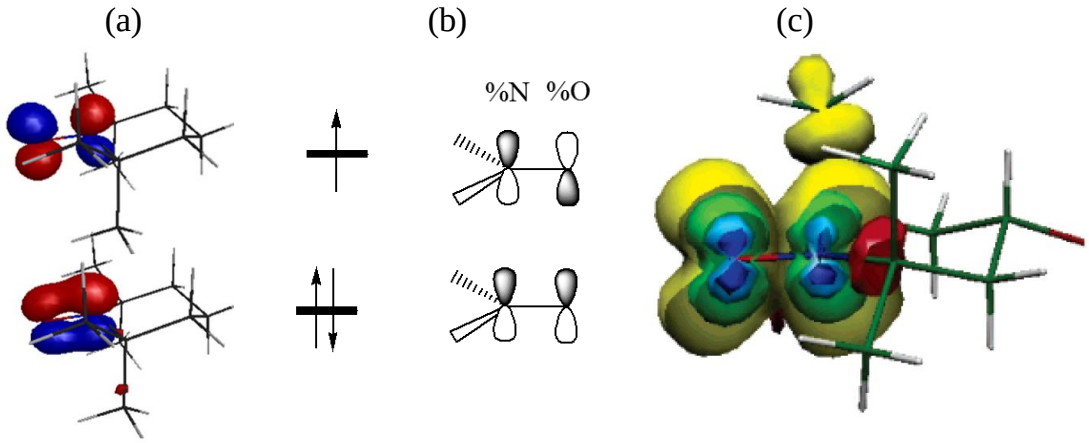

Figure I.2. The NO group as spin carrier. (a,b) The π-bonding and π^* - antibonding molecular orbitals; (c) spin density drawn at different iso-surface values, respectively, 0.1, 0.05, 0.025 and 0.005 electrons per $Å^3$.

The variation of the electronic exchange interaction (J), which depends on the distance and represents the through-space interaction between the two spins, can be visualized with the RES analysis using stable radicals, as is the case of the Figure I.3. For example, when the two nitroxides of a molecule are isolated (or large distance), the signal represented by the three lines derives from the coupling of the electron with the ^{14}N (I=1) nitrogen nucleus, generating $2I$+1=3 intermediate states. When the exchange coupling is sizeable ($J>>A_N$, $J/A_N>5$), a signal of five lines will appear [15].

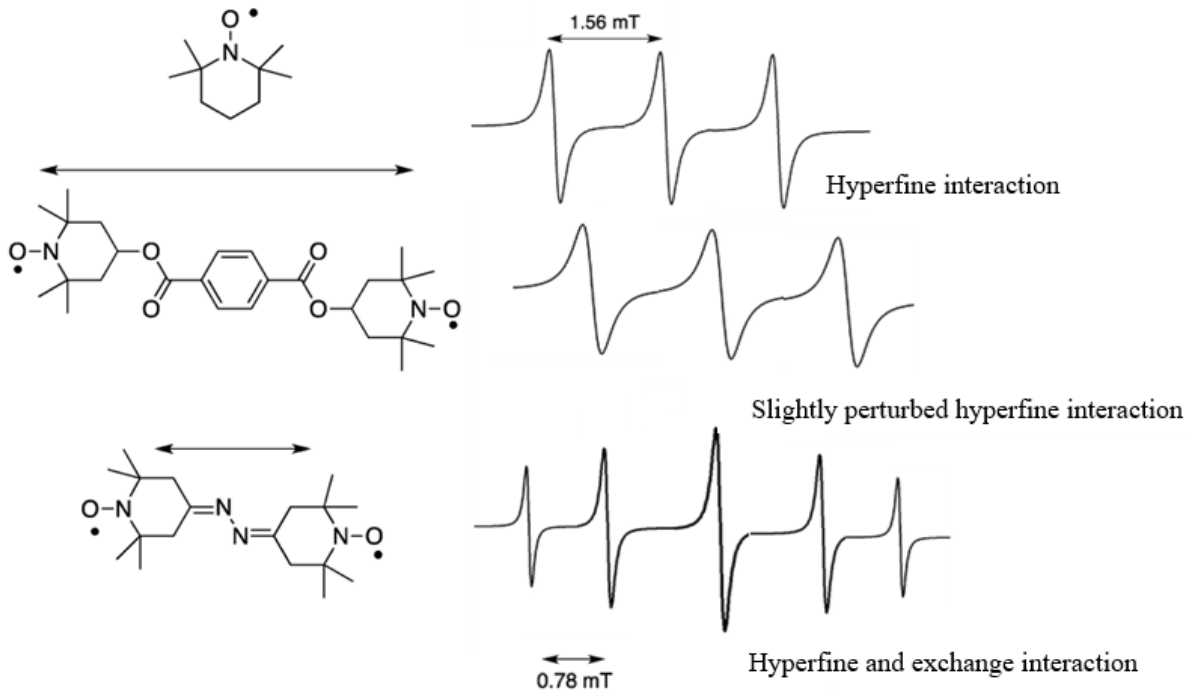

Figure I.3. Qualitative representation of RES patterns in TEMPO-based biradicals. From top to down: triplet due to hyperfine coupling, quasi-independent spin carriers (slightly perturbed hyperfine spectra) and hyperfine coupling imbricated with strong exchange interaction. ***Adapted from*** *M. Abe, Chem. Rev. 2013, 113(9), 7011–7088.*

In the following we will briefly illustrate the power of modeling methods, as complements to experimental techniques, the message of this work being that the calculation can offer useful information on subtle details that are not directly available from experiment, serving, in feed-back to a better exploitation of the instrumental data themselves.

The most exploited computational method, throughout this work, as well as in the actual literature state of art, is based on the Density Functional Theory (DFT) [16]. In the frame of this method there are specific variations, such as the Broken-Symmetry (BS) approach [17,18] for the estimation of the exchange coupling or the so-called Time Dependent (TD) DFT for the simulation of electronic spectra [19]. Knowing the intrinsic limitation of the DFT, in certain circumstances we employed also other types of methods, such as Complete Active Space Self-Consistent Field (CASSCF) [20] or Valence Bond (VB) [21]. A particular emphasis is that the VB method is very akin to the concepts related with the HDvV spin Hamiltonian, being also a very meaningful approach to general issues of the chemical bonding.

ORIGINAL CONTRIBUTIONS

Chapter II

Stable Organic Radicals. Structural considerations

II.a. Magneto-structural correlations in idealised dimeric systems with nitroxide-type spin carriers. Spin coupling rationalization from the point of view of the orbital overlap in pairs of nitroxide radicals. The role of the solvent in mediating the spin coupling.

This second chapter presents different case studies meant to analyse the connection between the molecular structure and spin properties of systems based on the TEMPO radical as a spin carrier [22]. The first half of this chapter is about the variation of the coupling parameter, *J*, in systems containing two spin carriers. For the beginning, we will consider a simple idealised system: two TEMPO molecules in vacuum, taken in different configurations, as is illustrated in the Figure II.1. In the Configuration 1, where the TEMPO molecules are mutually perpendicular, the π-type overlap vanishes, expecting then to have a positive exchange coupling parameter (ferromagnetic). When the two fragments are in the same averaged plane, as is the case for Configuration 2, one finds antiferro coupling, by the predominance of negative terms factored by the reaching of a maximal orbital overlap.

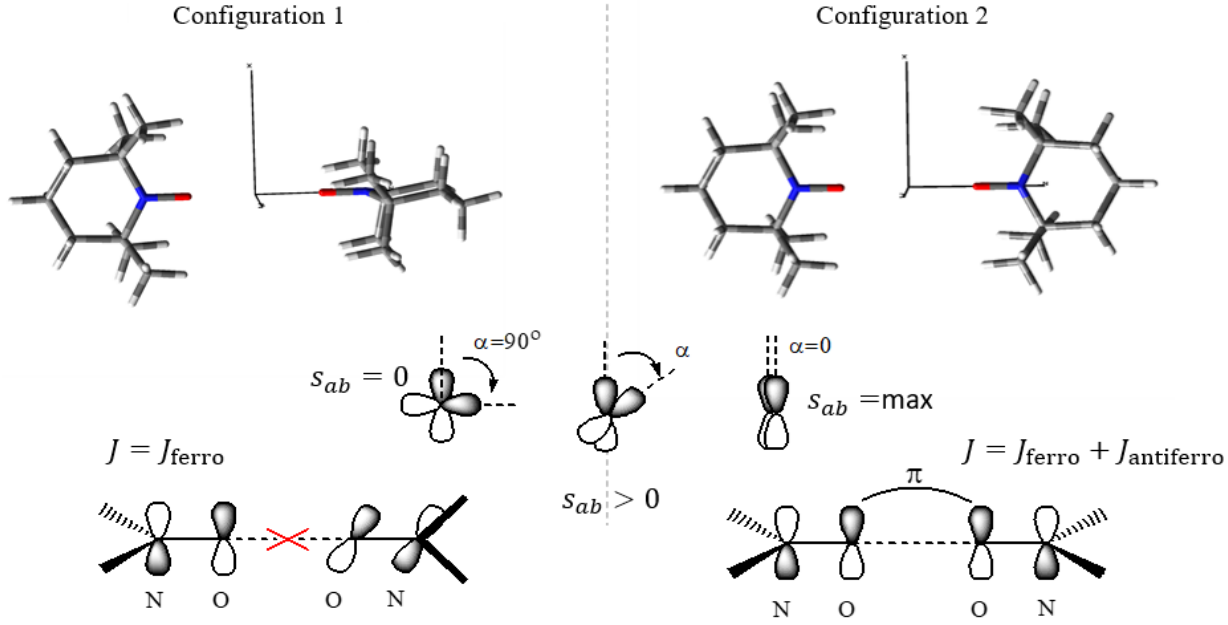

Figure II.1. The two geometric configurations proposed for the TEMPO pairs: Configuration 1- in the left side, Configuration 2- in the right side. The inset represents the angles between the *p* orbitals, along the N-O axes.

For a better understanding of the solvent role mediating the exchange coupling, we placed a molecule of dichloromethane between the TEMPO moieties, the Figure II.2 presenting the

proposed orientations of the solvent. We labelled by ‘a’ the case where the solvent is the placed with the chlorine atoms near the NO groups, and by ‘b’ the configuration with the ClCCl plane perpendicular on the NO group axes. For the calculation of the exchange parameter, *J*, we used the Broken-Symmetry approach, in the DFT frame [16], applying the Yamaguchi and Onishi [23,24] formula:

$$J = -\frac{E_{HS}-E_{BS}}{\langle S^2\rangle_{HS}-\langle S^2\rangle_{BS}} \quad , \text{(II.1)}$$

where HS denotes the High Spin configuration, and BS stands for the Broken-Symmetry one.

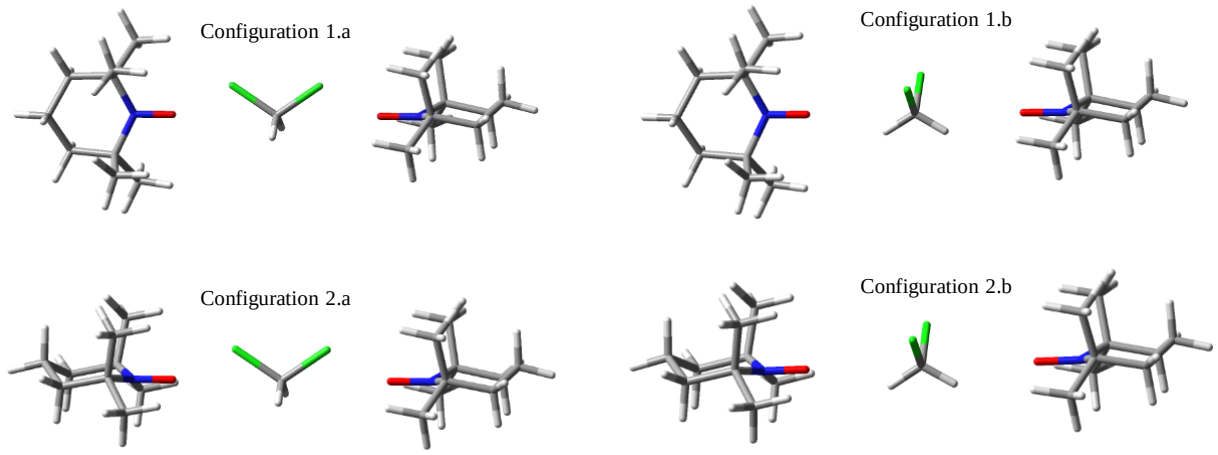

Figure II.2. Molecular orientation in the complexes including a CH_2Cl_2 molecule between two TEMPO radicals. The representation corresponds to an O…O separation of 7 Å between radicals.

The results from the BS-DFT calculations are illustrated in Figure II.3. In this figure, one may see the variation of the exchange coupling as function of the oxygen-oxygen distance between the two TEMPO radicals. The absolute values of the spin coupling are decreasing with the O…O distance, the dependence being exponential. The main graphs show, with dashed lines, the solvent added “from keyboard”, through the Self Consistent Reaction Field (SCRF) approximation, as implemented in Gaussian09 program [25], testing here the built-in parameters for dichloromethane. The computed points and fitted lines for the radicals in emulated solvent environment are not much departed from those resulted in vacuum. This means that the SCRF method is not appropriate for the approximation of the exchange coupling parameter in solvent environments. The insets show the exchange coupling computed when the solvent is added as a real CH_2Cl_2 molecule, placed in between the NO groups. The results are very different from those with the “keyboard” solvent, the absolute values increasing very much (green and violet lines, on the left, respectively right abscissas). E.g. if take a look at the inset from the right side of the figure, at the violet line, we may notice that the lowest value is -1500 cm^{-1}, while in vacuum (one the main right-side graph) was -20 cm^{-1}. In the inset from the left side of the figure, one notes, for the green line, the mutation of the exchange coupling sign, from ferro to antiferromagnetic.

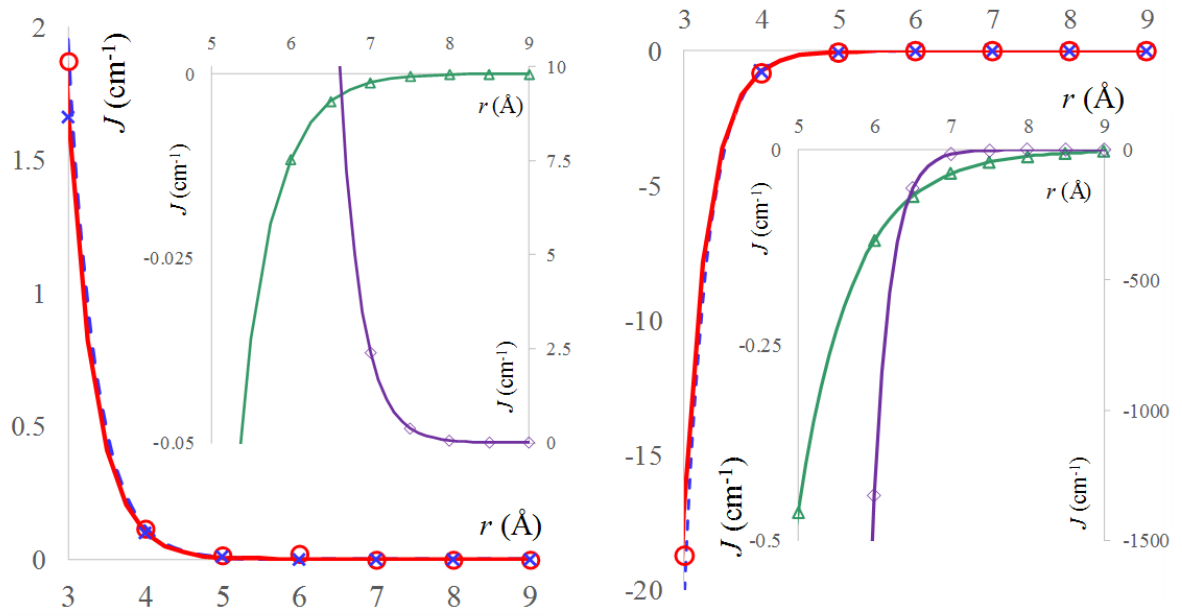

Figure II.3. The computed and fitted curves for the variation of exchange coupling, $J(r)$, as function of oxygen-oxygen distance (r) between two TEMPO radicals, taken in the Configuration 1 (left side) and Configuration 2 (right side). The circle symbols (o) correspond to computed BS-DFT data, the continuous red lines represent the fitted exponential dependences. The (×) symbol stands for similar data, computed with BS-DFT data and SCRF solvent model, while the dashed blue lines are the corresponding fit. The insets show the results of BS-DFT calculations with true solvent molecules placed at conventional orientations between radicals. The diamond symbols and violet lines correspond respectively to computed and fitted data in the case of a solvent arranged with the CCl_2 moiety in the same plane with the NO…Cl ones; the J values are represented on the right-side abscissa of each inset. The triangle symbols and green lines represent the coplanar CH_2 and NO...H moieties; the representation refers to the left-side abscissas of the insets.

When the NO groups are kept collinear, while a TEMPO molecule is rotated around the axis to obtain the angle between the *p* lobes, the overlap integral varies as in the formula $S_{ab} = S_{ab}^0 \cdot \cos(\alpha)$. Thus, at a certain r distance between the oxygen atoms, one may infer the following dependence of the exchange integral on the α angle like:

$$J(r,\alpha) = J_F(r) + J_{AF}^0(r)\cos(\alpha)^2 \,. \qquad \text{(II.2)}$$

The results fitted with the above-mentioned equation and the calculated data are represented in the graph from Figure II. 4. If we rescale the margins of each curve $J(r, \alpha)$ *vs.* α at the same extreme values, then the patterns for distinct r values are becoming similar. The maximum and minimum values of the J parameters are decreasing with the distance.

In practically all the cases, the dependence on distance can be fitted in exponential form:

$$J(r) = j^0 \cdot \exp(-a \cdot r) \qquad . \qquad \text{(II.3)}$$

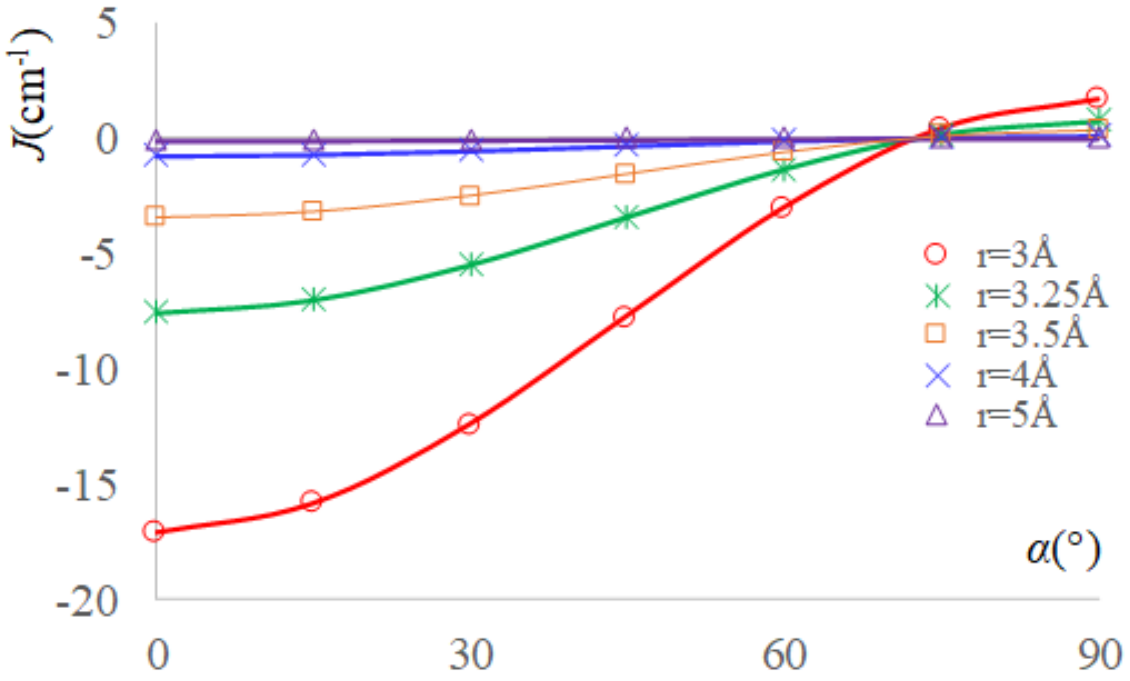

Figure II.4. The exchange **i**ntegrals as function of the α angle between *p*-type lobes for a TEMPO dimer coaxial NO groups. The marked points correspond to the BS-DFT calculated data and the continuous lines are fitted with the equation II.2, with previously fitted $J_F(r)$ and $J_{AF}^0(r)$ parameters.

We repeated the same numerical experiment of rotating the TEMPO molecule around the axis, inserting a CH_2Cl_2 molecule in the middle of the two spin carriers. The results are illustrated in the Figure II.5. Surprisingly, the solvent intervention does not affect too much the trigonometric regularity as function of the α angle.

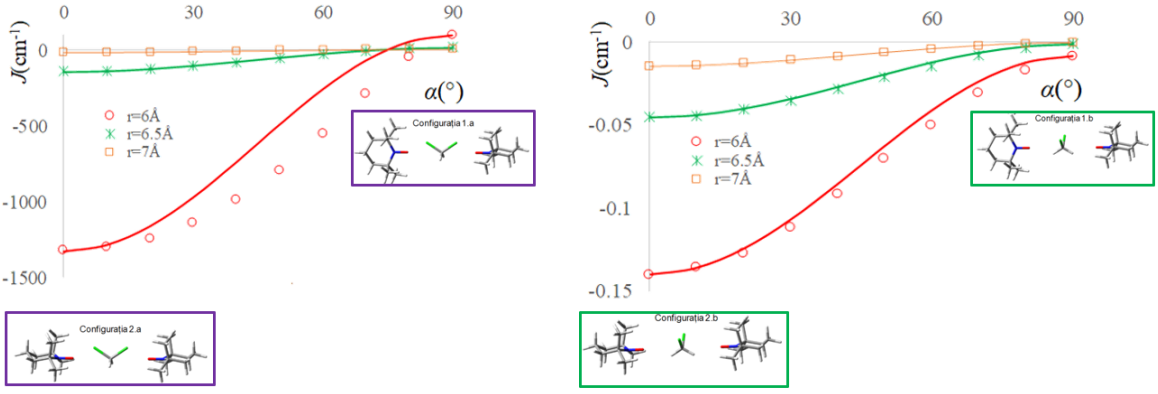

Figure II.5. The exchange **i**ntegrals as function of the α angle between *p*-type lobes for a TEMPO dimer coaxial NO groups, after inserting in between a CH_2Cl_2 molecule. The geometry miniatures are same shown in Figure II.2. Note the approximate retaining of the same pattern of $J(r, \alpha)$ *vs*. α curves as discussed for Figure II.4.

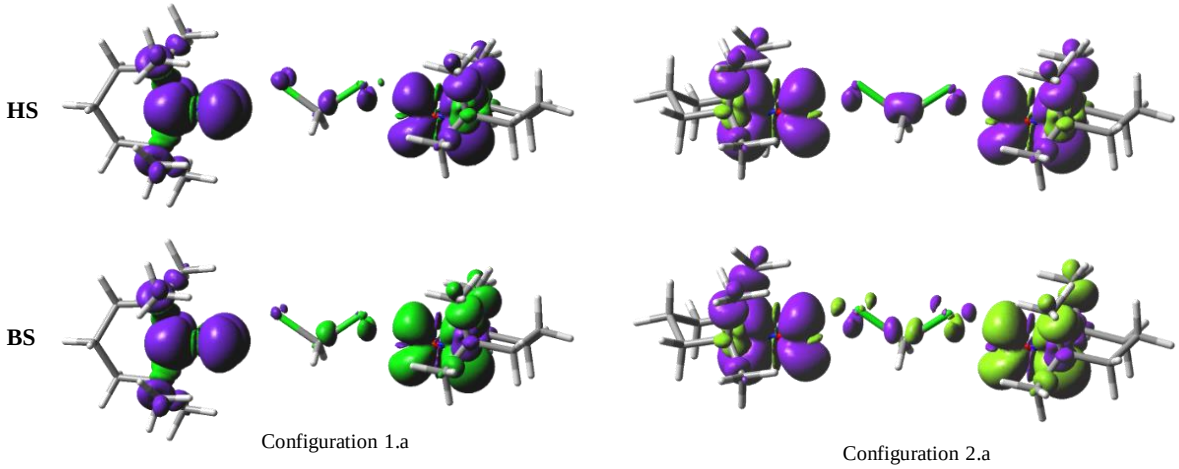

Figure II.6a. The spin density maps, as 0.001 e/Å^3 isosurfaces, for the 1.a and 2.a configurations, at the *r*=7 Å separation between the oxygen atoms of the colinear NO groups, with the oxygen atoms in the vicinity of the chlorine atoms of the dichloromethane molecule. The upper part shows the predominant α density of the triplet configuration, labelled HS (High Spin). The lower half shows the Broken Symmetry (BS) configuration. The violet and green colours correspond to the respective α and β spin densities.

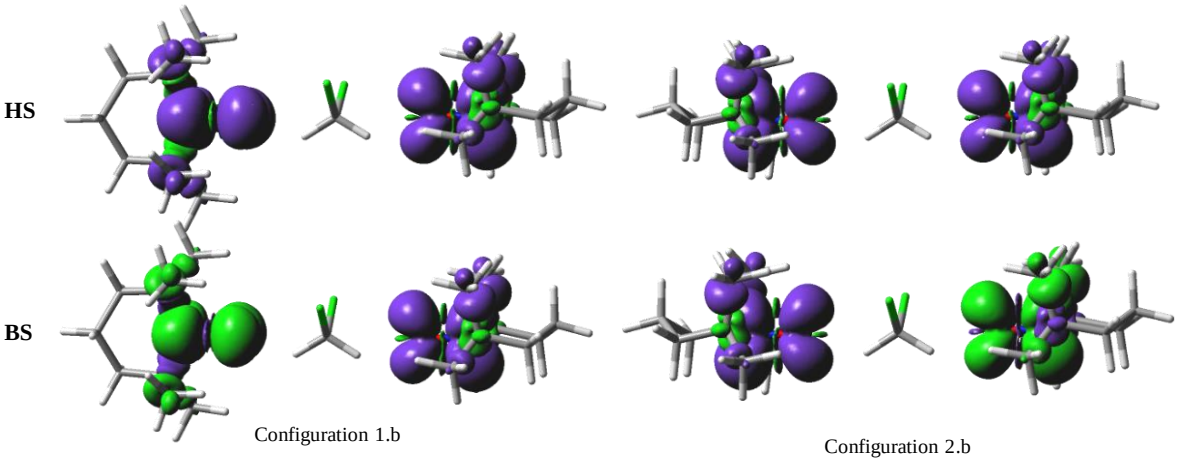

Figure II.6b. The spin density maps for the 1.b and 2.b configurations, at the *r*=6 Å separation between the oxygen atoms of the colinear NO groups, with the oxygen atoms in the vicinity of the hydrogen atoms of the dichloromethane molecule.

To understand the mechanisms of mediation exerted by the solvent, we analysed the spin density distribution and the spin density difference maps in the computed complexes, after subtracting the clouds of the standalone solvent and those of the TEMPO dimers (as converged in the through-space interaction cases). The spin density maps are illustrated in Figures II.6. The partial density over the solvent suggests that the CCl_2 moiety is able transmit the exchange coupling, by delocalization through the virtual orbitals ported by the chlorine atoms, the mechanism being a donor-acceptor relation of the respective oxygen-chlorine contacts. Although not favourable from energy point of view, such contacts can occur enforcedly during the solvent dynamics.

II.b. The dipolar coupling and the solvent effect. Basis sets and the hyperfine coupling

The second half of this chapter continues with the analysis of other EPR parameters, namely the Zero-Field Splitting (ZFS) due to dipolar effects and the hyperfine coupling. First, we checked by computation the pattern of the ZFS parameters, taking the same molecular models as in the previous section, interacting through-space or *via* a dichloromethane molecule. The results, produced with the B3LYP functional and EPR-II basis, are shown in the Figure II.7, considering the Configuration 2 of two TEMPO molecules. The calculation with fake SCRF-type solvent gives almost the same results as in vacuum. At the same time, the real solvent molecule placed in between does not affect very much the variation of the dipolar coupling parameter, the solvent seeming almost "transparent" to this sort of interaction.

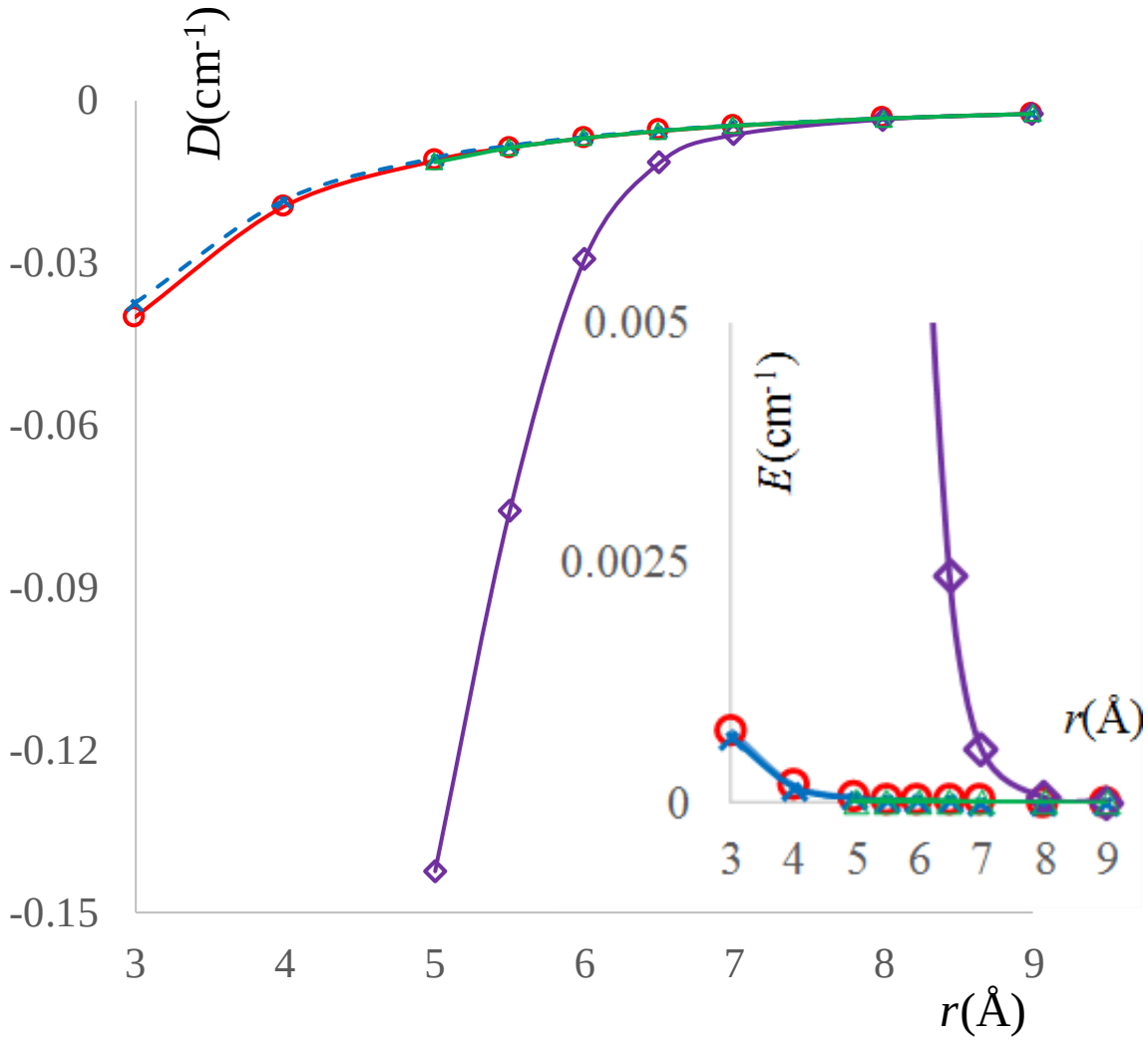

Figure II.7. The ZFS parameters computed for Configuration 2, as function of separation between the oxygen atoms of the colinear NO groups. The main panel shows the variation of the *D* parameter for: two TEMPO molecules in vacuum (red line and open circles); with SCRF solvent option (dashed light blue lines and × symbols); two TEMPO molecules with a CH_2Cl_2 solvent in between, having the CCl_2 and NO…Cl sequences coplanar (Configuration 2.a-violet line and diamond symbols); two TEMPO molecules with solvent oriented with coplanar CH_2 and NO…H parts (Configuration 2.b-green line and triangle symbols). The inset corresponds to the *E* parameter, drawn with the same conventions, for the respective symbols. The Configuration 1 shows a very similar variation of *D*, while the *E* is rigorously null, by symmetry reasons.

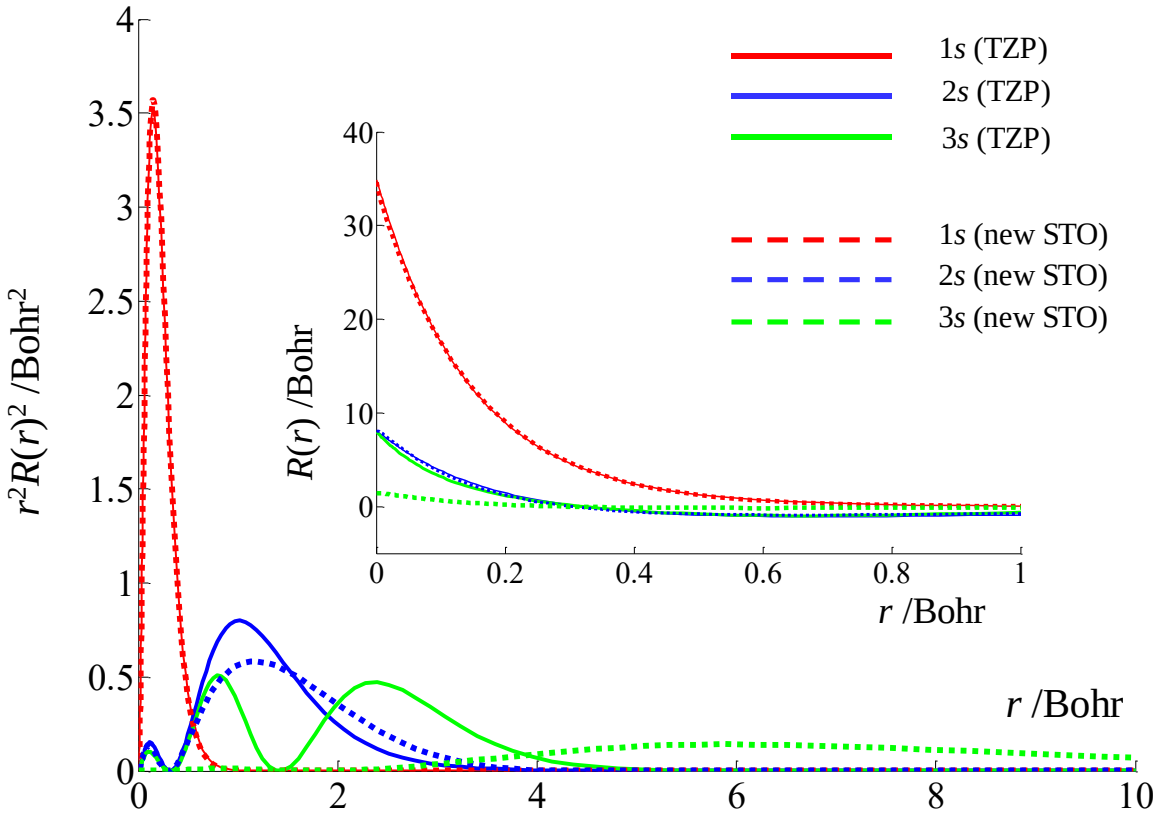

Figure II.8. Radial profiles of the 1s, 2s and 3s atomic orbitals of the nitrogen, computed with STO-type functions and BLYP functional in the ADF code. The continuous lines correspond to the standard TZP basis, the dashed lines illustrating preliminary tests with a new basis showing long-range maxima in the $r^2R(r)^2$ functions. The inset shows the *r vs.* $R(r)$ variation near nucleus.

In the problem of computing the hyperfine parameters, we realized the first steps in a pioneering breakthrough, designing new Slater Type Orbital (STO) basis sets with improved behaviour in the long-range domain, and also for the nuclear density. We worked in the Amsterdam Density Functional (ADF) environment. The main graph in Figure II.8, illustrating the case of nitrogen atom, shows that our new basis acquires extended range tails (in dashed lines), compared with the standard ADF-type basis named TZP (triple zeta and polarization), showing shrunk radial profiles for 2s and 3s. We tested that the better account of the distant zones improves the responsivity of computed hyperfine parameters to the environment, as is expected from experimental point of view. Besides, the zone close to the nuclei is better described, as seen in the inset from the Figure II.8. Thus, one expects that the values of functions at nucleus decreases in the 1s>2s>3s order, as obeyed by our new STO basis. In turn, the standard TZP shows accidental 2s~3s superposition, which is not reasonable.

II.c. Supramolecular interactions in host-guest systems (cyclodextrins and nitroxide radicals)

We also dealt with issues of supramolecular encapsulation processes, prompted by the importance of such interactions in experiments involving spin probes. Here we considered the inclusion of a TEMPO radical in cucurbit[6]uril (labelled CB[6]) or the β-cyclodextrin (β-CD) toroidal molecules. We proposed a new methodology in the estimation of association energy, avoiding the questionable use of the so-called *counterpoise* calculations (or in other words, Basis Set Superposition Errors- BSSE).

Table 1. Molecular and complexation energies computed with plane-waves for the *AB*=TEMPO@β-CD system, as a function of the e_{cut} threshold. The data correspond to the complex optimized with PBE functional and Grimme D2 corrections. The values without the D2 treatment are obtained adding the +26.76 kcal/mol shift to all Δ*E* values.

e_{cut} (a.u.)	E_A (a.u.)	E_B (a.u.)	E_{AB} (a.u.)	Δ*E* (kcal/mol)
10	−89.808568	−843.193164	−933.080225	−49.255
15	−91.429465	−864.977950	−956.457872	−31.662
20	−92.003204	−874.457998	−966.508544	−29.707
25	−92.155612	−877.393910	−969.588669	−24.565
30	−92.187830	−878.113239	−970.339341	−24.016
35	−92.193473	−878.238044	−970.469690	−23.954
40	−92.195163	−878.253100	−970.486430	−23.950
…	…	…	…	…
∞	−92.213100	−878.724000	−970.972000	−21.900

In this view, we turned to the use of plane-wave (PW) methods. Usually, these are employed by physicists in solid-state band structure calculation, but can be adapted also for molecular calculations, in the so-called Gamma-only setting, provide that the unit cell containing the molecule is sufficiently large. In a PW calculation, the quality of the basis is tuned by an energy cut-off parameter, (e_{cut}). Our simple, but yet pioneering idea, in the purpose of supramolecular assemblies, is that after testing a series of e_{cut} parameters, the resulting molecular or formation energies can be fitted with a smoothly convergent exponential function, which, extrapolated at the $e_{cut} \rightarrow \infty$ case, emulates the situation of the ideal best basis set. We illustrate in Table 1, such a treatment for the cyclodextrin-TEMPO complex.

We also carried critical discussion comparing the results extrapolated at infinite precision of the basis sets with BSSE calculations performed with various Gaussian-type bases, evidencing their non-systematic behaviour.

Chapter III

Nitroxide-based radical systems in complex and dynamic environments

III.a. Use of nitroxide biradicals in nano-chemistry. Synthesis and instrumental monitoring of gold nanoparticles. EPR measurements. Spin probes in the albumin-nanoparticle systems

In this chapter, we illustrate an experimental application of selected mono- and bi-radicals derived from TEMPO [26], continuing then with related structural considerations. The EPR of spin probes are corroborated with a plethora of other techniques, in order to monitor the formation and growth of gold nanoparticles in environments containing biomolecules. These parallels numerous case studies concerning the therapeutic use of gold nanoparticles [27,28]. It was shown that proteins can assist the formation of nanoparticles [29], particular situations involving albumins [30,31]. In the following, we will focus on bovine serum albumin (BSA), as initiator of gold salts reduction [32-34].

The BSA sample is dissolved in $HAuCl_4$ (2×10^{-3} M) solution, under phosphate buffer, then let to evolve at room temperature, for a month. The evolution of the protein can be tracked by circular dichroism, sensing the global changes in secondary structure, while the gold particles can be directly detected by the UV-VIS recording on the colloid, observing the so-called plasmonic band (determined by delocalized electrons at the metallic surfaces), which induces a specific violet colouring. The formation of nanoparticles is visible, at end, by the Transmission Electron Microscopy (TEM) technique.

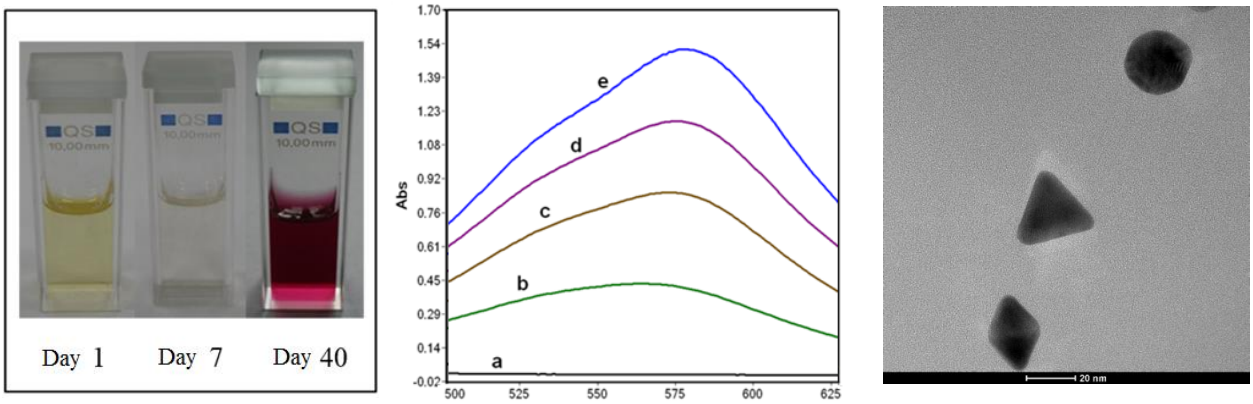

Figure III.1. Synopsis of gold particle formation in BSA environment. Left panel: colour of samples (from initial solution to colloids showing plasmonic bands); middle panel: the spectral record of the sample showing the growth of plasmonic band (a-initial, b-3 days, c-1 week, d-2 weeks, e-3 weeks); right-side: TEM image of gold nanoparticles.

The figure III.1 shows images of the samples in different stages, altogether with UV-VIS spectra monitoring the specific plasmon band and a selected TEM picture of the formed nanoparticles. One may observe here diamond-shaped, triangular and circular profiles, which are

probably projections of particles with respective octahedral, pyramidal and quasi-spherical shape. The average diameter of the particles in the displayed stage is between 15-20 nm.

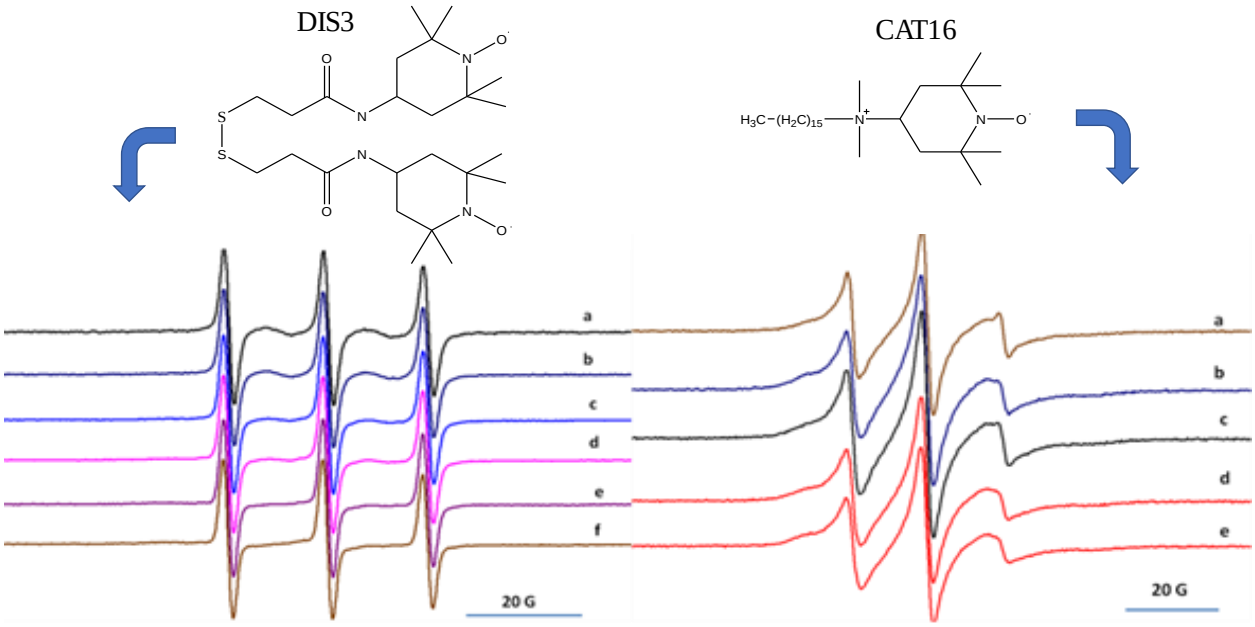

Figure III.2. The used spin probes. The biradical labelled DIS3 shows affinity for the gold nanoparticles, while the cationic radical CAT16 is adequate for monitoring the protein structure. Left-bottom side: (a to f) the EPR spectra of DIS3 for the respective sequence of {0, 4, 6, 10, 13, 17} days; right-bottom side (a to e) the EPR spectra of CAT16 at {0, 4, 10, 13, 17} days, respectively.

The spin label CAT16 (4-N,N-dimethyl-hexadecyl-ammonium-2,2,6,6-tetramethyl-piperidin-1-oxyl iodide) is a cationic quaternary ammonium salt having one substituent made of a sixteen carbon atoms linear catena, while another one by the TEMPO moiety. It shows affinity towards the BSA, by multiple factors: the cationic end approaches the negatively charged parts of the protein, while the carbon catena finds hydrophobic sequences in the macromolecular structure. Intuitively, is easy to imagine that the long tail of the spin probe gets entangled with the folded bio-molecule, avoiding the water solvent surroundings. Then, glued to the BSA, the evolution of CAT16 signal reports the modification of macromolecule in the environment, a series of EPR curves -at different stages- being shown in the right-bottom corner of Figure III.2. The complex profile is probably due to the superposition of various signals of radicals attached to different parts of the BSA. At the same time, the pattern suggests restricted movements of the spin carriers, as expected if consider the probes well embedded in the BSA. The variation along time, paralleling the growth of gold nanoparticles, shows relatively little changes, suggesting that the proteins are not much affected in the process.

The DIS3 probe is a biradical consisting in identical halves, connected by a sulphur-sulphur bond. This probe „spies" the formation of the gold nano-particles, considering its aurophilic nature.

Namely, the S-S bonds are dissociating, forming Au-S bonds on the surface of the cluster, turning then the biradicals in disjunct mono-radical spin probes. The EPR profiles are evolving with the growth of the particles, as shown in the left-bottom side of the Figure III.2. At the beginning, the major three signals due to the hyperfine splitting are interlaced with two larger bands, placed in between, indicative of weak exchange coupling. In time, these details are vanishing, the intervals between hyperfine peaks remaining flat. This can be interpreted as the decoupling of the initial exchange, because the growing particles are determining larger separations between the radicals „planted" on their surface (if the concentration of the spin probe is kept constant). Thus, with the appropriate spin probe, one may collect information from the different components of a complex system.

III.b. Modeling flexible biradical systems

Although we cannot match by modeling the complexity of the phenomena implied in the use of spin probes in studies like previously illustrated, we will attempt first steps in such a direction, performing computational analyses on the biradicals shown in the Figure III.3. The systems are consisting in 4-amino-TEMPO groups grafted on aromatic cores [35], respectively on benzene 1,3 di-sulfonyl, in the system labelled (**1**), and on the dibenzo furane-2,8-di-sulfonyl moiety, for the biradical named (**2**). The same figure shows also the EPR spectra in dichloro-methane, the signals placed in the two spaces of the hyperfine triplet suggesting significant exchange coupling, a fact that will be tested by computational experiments.

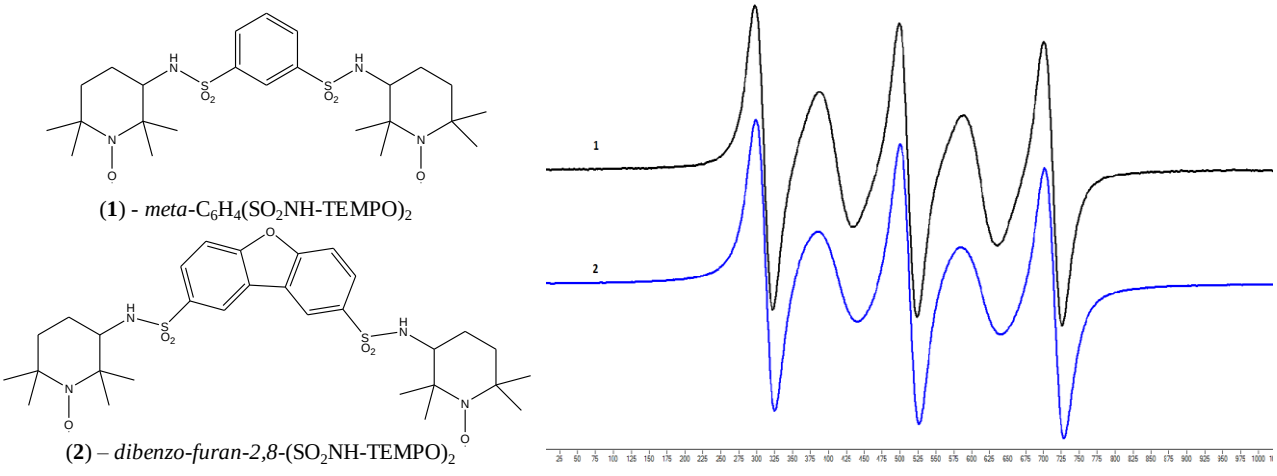

Figure III.3. The biradicals labelled **1** and **2**, altogether with their EPR experimental spectra.

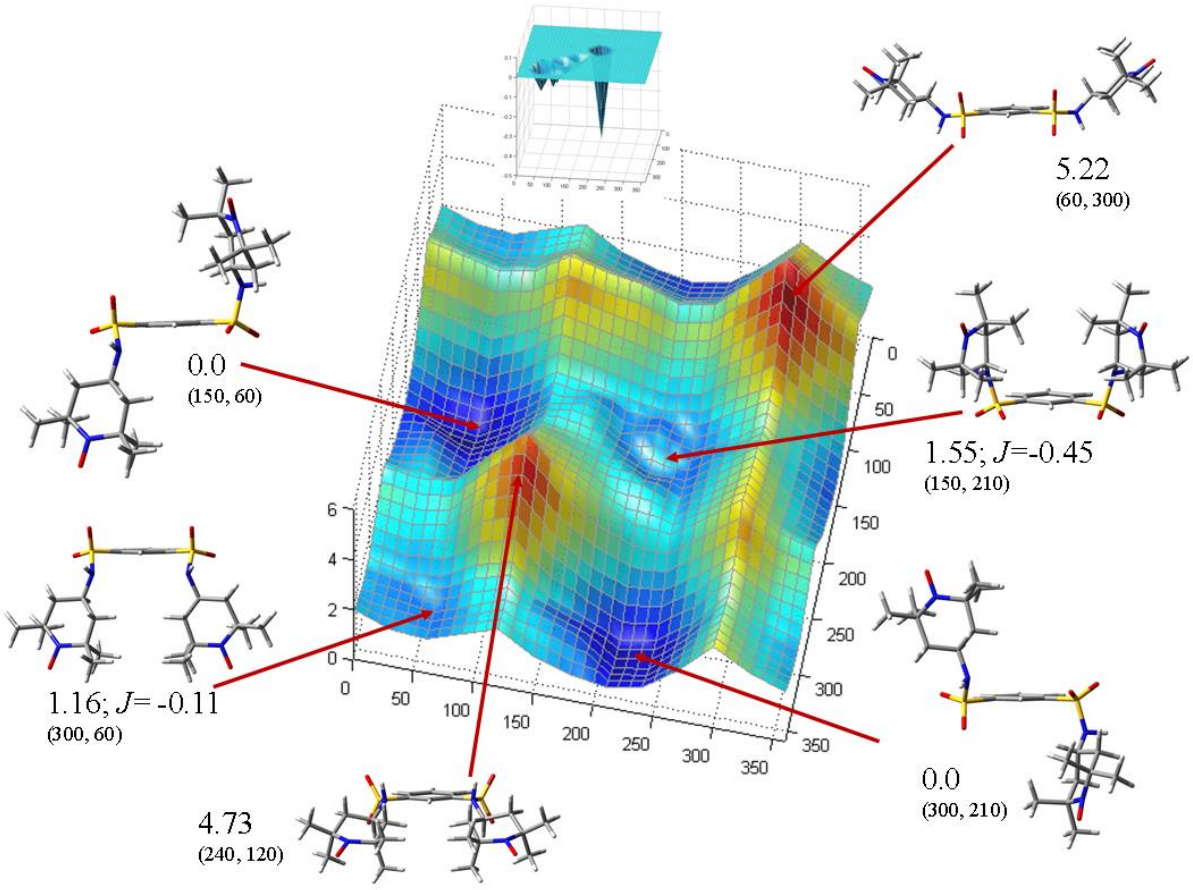

Figure III.4. Relaxed potential energy surfaces resulted from the scan of the C-C-S-O dihedral angles (denoted τ_1 and τ_2) branching the TEMPO fragments to the central core, with excerpts of molecular structures at extrema points. The associated values are the relative energies in kcal/mol (with 0 for the minimum) and the computed exchange coupling parameters (in cm^{-1}). The printed parentheses are τ_1 and τ_2 at the corresponding grid points.

Here we illustrate only the case of compound **1**, the other congener behaving qualitatively similar. We considered that the most important degrees of freedom are the related with the rotation of the sulfonyl groups around the aromatic trunk, selecting then as active parameter the C1-C2-S-O and C1-C6-S-O dihedrals, where the labelling of the carbon atoms follows the standard count for substituted benzene rings. In other words, the C1 corresponds to the CH group placed between the sulfonyl substituents. The two dihedral angles, denoted by τ_1 and τ_2, are topologically equivalent, but can vary independently, generating the energy landscape depicted in the Figure III.3. The absolute minima correspond to the *anti* placement of the rotated TEMPO groups with respect of the central benzenic ring. However, other conformations with *syn* pattern, corresponding to maxima or relative minima, are spaced by low energy value (at most 5.22 kcal/mol), so that these structures are easily affordable. The above simulation is done in vacuum (with the B3LYP/6-31G* setting), the results with solvent emulated by SCRF increments being qualitatively similar.

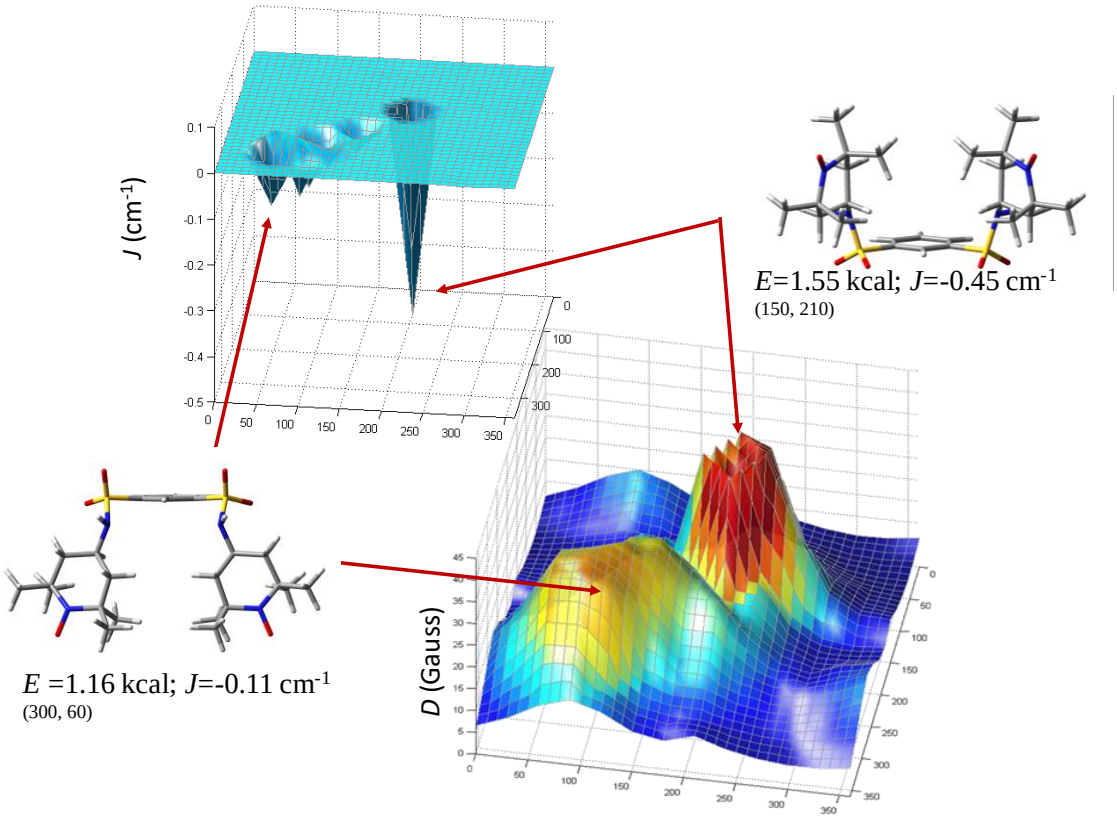

Figure III.5. The map of *J* and *D*, parameters computed on the same geometry domain as described for the previous figure.

The computed exchange (*J*) and dipolar (*D*) parameters are mapped for the same geometry sets that resulted from the above relaxed potential energy surface, being shown in the Figure III.5. The exchange parameters for the selected extremum conformations were also annotated in the precedent graphic, from Figure III.4. One observes that for the cases with close encounter of the NO radical groups, the exchange parameter records sizeable values, being negative in sign (i.e. antiferromagnetic spin ordering). For instance, a J=-0.45 cm^{-1} value is reached at a conformation with relative energy 1.55 kcal/mol, which is, in principle, easily attainable during the dynamics in solution. The ZFS-type parameter, *D*, gets also relatively significant magnitudes (up to about 40 Gauss) on the scanned domain. As discussed previously, the SCRF modules are not helpful for mimicking the solvent role on the exchange coupling. At the same time, we showed that the solvent, accounted quantum mechanically can amplify certain exchange paths. Therefore, one may prolong qualitatively the results of the modeling in vacuum, assuming that, in a solvent surrounding, the map of exchange coupling can be sensibly enhanced. Thus, we got, by modeling, a justification for the experimentally detected exchange coupling.

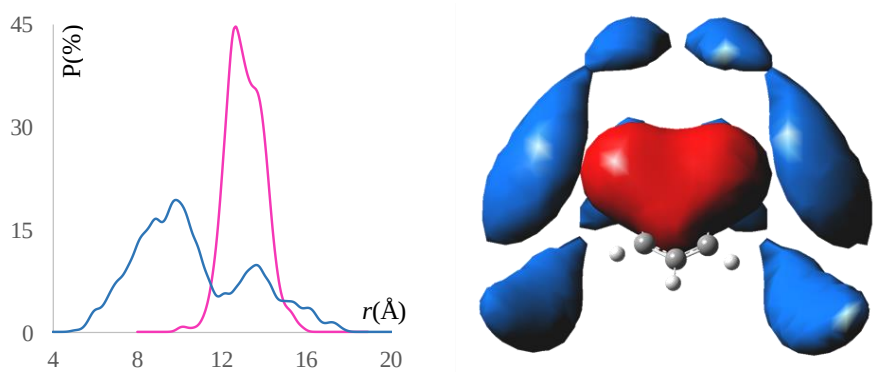

Figure III.6. Distribution of the O…O distance between the two spin carriers of biradical (**1**), TEMPO-$NHSO_2$-C_6H_4-SO_2NH-TEMPO, from molecular dynamic simulation (*vide infra*). Blue line: the biradical in vacuum, pink line: the biradical in CH_2Cl_2. The density of probability of the barycentre placement of the two NO bonds (blue) and the middle point between the two NO groups (red contour), as resulted from the molecular dynamics in CH_2Cl_2 solvent.

A hint on the role of the solvent is obtained by recourse to molecular dynamics, taken in the simplified frame of the molecular mechanics. We considered a cubic box with the 30 Å edge, containing 248 CH_2Cl_2 molecules and one molecule of biradical **1**. A force field containing all the needed intra- and inter-molecular parameters was identified to be *oplsaa* [36], practically the sole option in the given circumstances. Using the *Tinker* code [37] for empirical molecular dynamics, and performing further handling of the black-box data by home-made codes, we reached conclusions distilled in the graphics from Figure III.6. Taking the radical position at the middle of the NO bonds, we drawn the averaged inter-radical distance in vacuum *vs.* dichloromethane. A glance at the left side of the Figure III.6 shows that the solvent narrows the distance to a domain of larger mutual separations, centred at about 14 Å, the value suggesting that the geometries may pertain to *anti*-type conformation. For a clearer resolution, we represented, in the right side of the Figure III.6, the spatial distribution probability of other two geometry parameters. The blue surfaces correspond to the position of individual radicals, with respect of the central benzenic ring. The four equivalent lobes correspond to equal probability of each TEMPO to be "above" or "below" the benzene plane, as well as the fact that the two radical branches are topologically equivalent. The red contour draws the preferred placement for the middle of the line drawn between the two radical carriers. The fact that this family of points falls in the centre of the molecule (over the benzene area) shows that the most frequent mutual placement is *anti*. If the *syn* conformations were more frequent, then two red ellipsoids, above and below the benzene, would have been expected. The above results are partial conclusions that deserve further development, which, corroborated with pedantic studies developed in the Chapter II on idealized cases, can bring a new light in the spin chemistry of nitroxide-based spin probes.

Chapter IV

Unstable Organic Radicals. Polyaromatic compounds with spin

IV.a. Triangulenes, graphenic fragments with spin

This chapter is devoted to carbon-based aromatic radicals belonging to a special class, described as graphenic fragments with triangular symmetry [38]. Our focus on this area emerges from previous preoccupations [39], considering also that the EPR on radicals from polyaromatic hydrocarbons is a distinct topic, corroborated with the new wave of interest for carbon materials boosted by the recent discovery of graphenes [40,41] The considered systems belong to the topologically induced spin [42,43], namely to the cases when the attempt to draw resonance structures with single and double bonds is not possible without introducing unpaired spins.

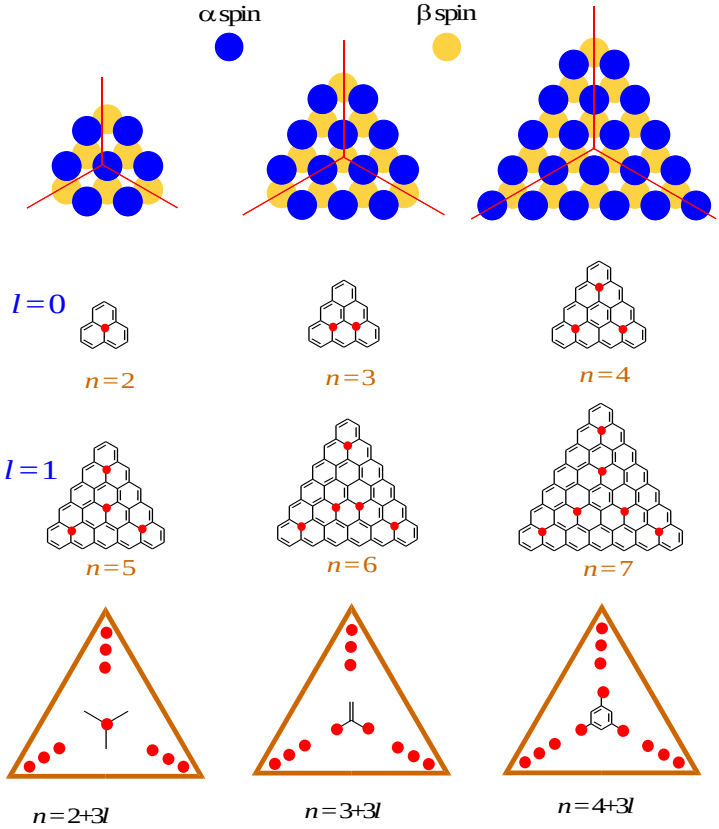

Figure IV.1. The scheme of structures and spin count in triangular graphene-type molecules. The systems can be classified by the number n of hexagonal units at one edge, being conventionally named *n*-triangulenes. There are three equivalency classes, with respective *n*=2, 5 .. 2+3*l*, *n*=3, 6 .. 3+3*l*, and *n*=4, 7 .. 42+3*l*, rings on edge (with *l*=0, 1, 2 etc). The bottom row shows the pattern of the distribution in the resonance structures with highest symmetry, while the top row suggests the bonding as alternation of α and β spin polarization, resulting in a net excess of β spins (*n*-1 for a given *n*-triangulene).

The charts drawn in the Figure IV.1 are illustrating this situation for the considered class of hydrocarbons, which will be generically named triangulenes [44]. Denoting by *n* the number of benzenic rings at one edge of the molecular triangle, these molecules can be organized in three subclasses, displayed on columns, as function of the structural component placed in the gravity

centre and the figure of the resonance structure with highest possible symmetry. Hopefully, the drawings are self-explanatory in this sense, skipping here the details. Only the first two members of the series, i.e. n=2 and 3 are experimentally characterized, the former having many known derivatives [45,46], while the last one being recently proven by surface chemistry techniques [47]. However, the general characterization on the class is worthy, because the drawn conclusions have a more general relevance, considering that the spin can be induced in graphenes not only in regular triangular fragments, but also in irregular circumstances, containing a triangular corner or promontories of this sort.

Our methodological interest stems also from the idea of exploiting and extending the capabilities of spin-coupling effective Hamiltonians. Namely, the *ab initio* facet of the Heisenberg-Dirac-van Vleck operator is akin to the Valence Bond (VB) class of models. The VB methods are rarely used in the nowadays modeling, dominated by the appeal of relatively simple DFT procedures. However, the reward of VB use is the possibility of translating the wave function (which has a multiconfigurational nature) as combination of resonance structures, i.e. objects perceivable by the chemical intuition.

IV.b. *Ab initio* Valence Bond calculations for phenalenyl radical. Spin distribution and bond orders in selected triangular aromatic systems

We show in left side of Figure IV.2, the minimal list of resonances to be considered for the n=2 triangulene (named also phenalenyl radical). Without entering the details, let us point that such a list serves as a recipe for constructing the wavefunction, being therefore something more than an exercise in the playground of graph theories. If dichotomize the resonances in four equivalence classes, labelled by A-D in the left panel of Figure IV.2, the VB calculation show that the participation of each element under the given annotations correspond to the following weights: w_A=2.55%, w_B=4.75%, w_C=5.00% and w_D=6.06%, if the groundstate is considered. The excited states can also be characterized in the same way. The above resonance list considered only the spin flipping configurations, while keeping one electron on each carbon atoms and considering the antiparallel coupling only between bonded carbon atoms. The extended version of the VB calculations, called CASVB, considers all the possibilities to distribute the electrons of the π -type orbitals. In spite of different orbital treatments, the CASVB is, at end, equivalent with the CASSCF calculations, i.e. yielding identic spectra of states. An intermediate level of calculation uses the so-called complete Rumer basis (in this case, having 429 elements), which includes resonances with

lesser intuitive aspect, e.g. a double bond (or an arrow, in the actual convention) between distant, non-bonded, carbon atoms.

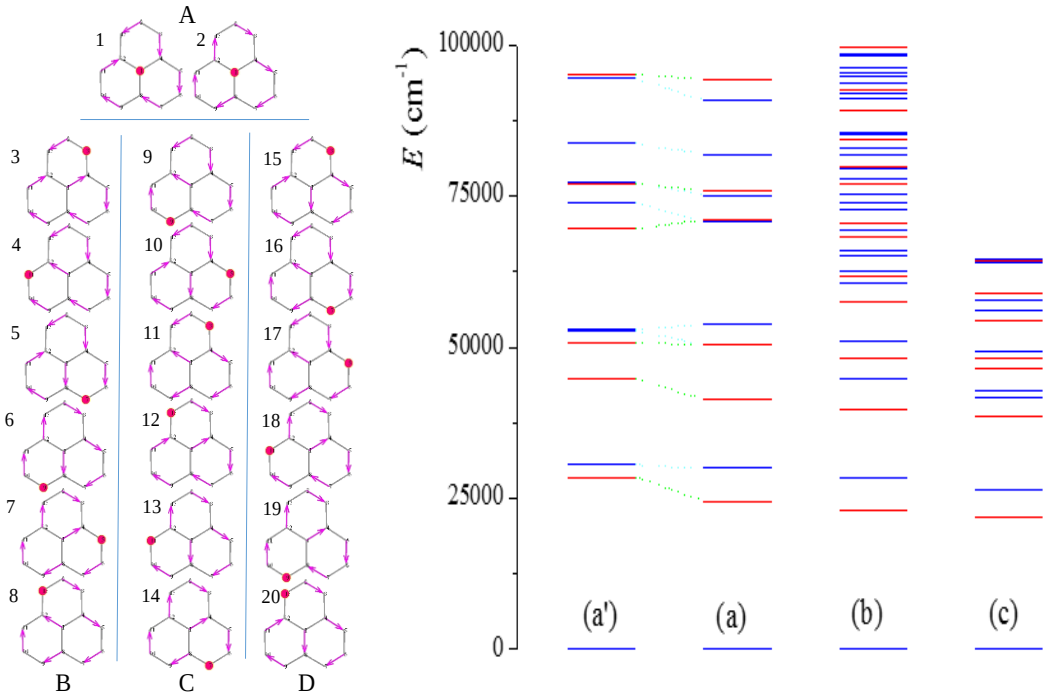

Figure IV.2. Left side: Minimal set of resonance structures for phenalenyl radical. Right side: Different multiconfigurational ways of accounting the states of the phenalenyl radical. The red lines denote doubly degenerate states, while blue the non-degenerate ones. (a) the VB calculation on the minimal list of resonances; (a') the fit of VB states from the (a) series with the HDvV phenomenological Hamiltonian; (b) the VB calculation with complete Rumer set, comprising 429 resonances (c) the first 20 states from CASSCF or CASVB calculations with 13 electrons in 13 π-type orbitals

On the edge of the technicalities related with such calculations, we introduce now some methodological innovations. The first step consists in fitting the HDvV Hamiltonian (shown in the introductory synopsis from Figure I.1) to the performed VB calculation. The match between (a') and (a) stacks of state energies from right side of Figure IV.2 illustrates the success of the fitting procedure. This figure contains in columns (b) and (c) results of extended sorts of calculations, from which we retain only that, irrespective the method, the sequence of about first four-five states results the same, concluding a relative trust in the methods belonging to the (a) and (a') type of treatments.

Skipping again details, we point that the *J* coupling parameters were taken in an exponential form, as function of carbon-carbon bond lengths, in a manner very similar with the distance-parameterized exchange coupling described in the Chapter II. The bond lengths are obtained from DFT-based optimization of the groundstate. Note that we can rely on DFT data, as long as we stay

on groundstate. The merit of VB calculations and related procedures described now, consists in the fact that we can account excited levels too.

The clue of the development is this: having a HDvV parameterization, we can emulate VB-alike results on relatively large polyaromatic radicals, while the proper *ab initio* VB or CASSCF treatments are becoming rapidly intractable with the size of the system. For instance, the *n*=3 triangulene is already prohibitive at this level. However, having the parameters calibrated, as briefly here described, on phenalenyl, we may emulate the electronic structure of higher systems.

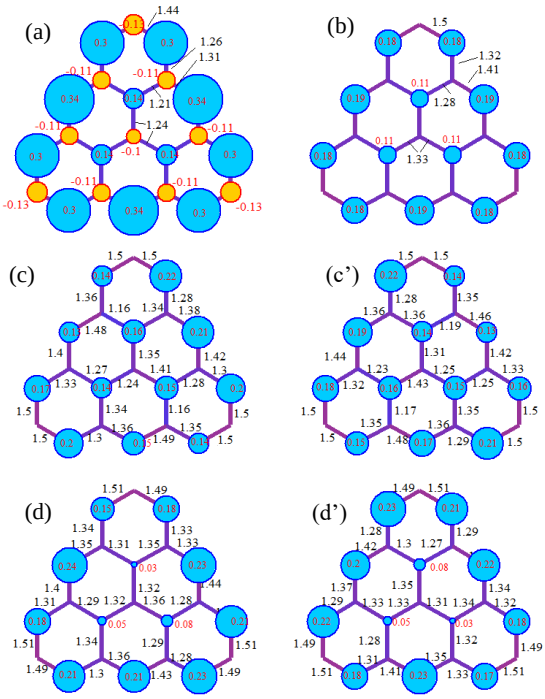

Figure IV.3. Spin densities and bond orders in the *n*=3 triangulene: (a) B3LYP ground state. (b) the VB spin model ground state, (c) and (c') VB model for the components of the doubly degenerate first excited state, (d) the doubly degenerate second excited state

The Figure IV.3 shows the spin distribution in the first few states of the *n*=3 triangulene. While the groundstate spin distribution can be obtained easily at the DFT level (shown the (a) chart), the excited states are not easy gains. A certain drawback of our modeling is that it can account only positive (restricted-type) spin densities (to be distinguished from unrestricted DFT results including spin polarization, i.e. nodes with negative tails of β-type spin density). However, considering that the α-type positive spin density is of first-rate importance, the model works satisfactorily, providing access to yet uncharted structure-property correlations, such as the possible spin-catalysis properties or even opto-electronics (once the excited states can be accounted) with carbon-based materials.

Chapter V

Metal ions systems. Spin Coupling and Electronic Paramagnetic Resonance Spectroscopy

V.a. Structure and spectroscopy in mixed ligands copper(II) complexes. Ligand Field Scheme. Rationalization of the EPR spectra.

In the following we will illustrate a correlation of the EPR parameters with structural data and electronic UV-VIS spectra in monomeric copper(II) complexes [48] having aromatic amines as lignands (namely pyrazoles and phenantroline). The discussed compounds are iso-structural, with pentacoordinate copper: $[(L^1)_2Cu(H_2O)(phen)](NO_3)$ and şi $[(L^2)_2Cu(H_2O)(phen)](NO_3)$ (**2**), where *phen* is the phenantroline, while, L^1 = 3,5-dimethyl-4-nitro-pyrazole şi L^2 = 3,5-dimethyl-4-iodo-pyrazole, the last ligands being synthesized by literature procedures [49]. In their relative structural simplicity, the discussed mononuclears are excellent case studies for revisiting qualitative and semi-quantitative aspects on Ligand Field (LF) modeling, corroborated with EPR and UV-VIS spectra, via computational explorations. In the following we will discuss only the data on compound **1**.

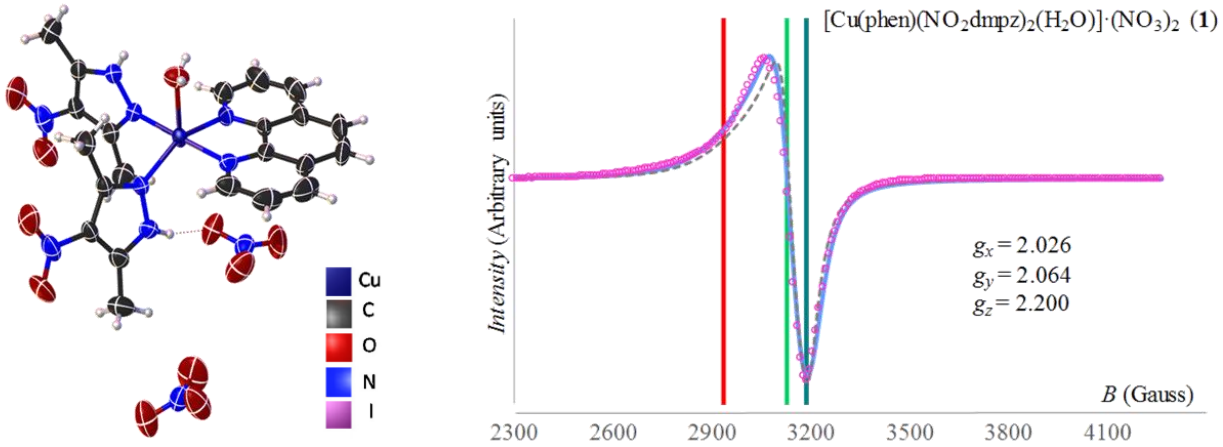

Figure V.1. Molecular units of the complexes and EPR spectrum (circles-experimental, continuous-fitted, dashed-fitted without hyperfine coupling) for compound **1**, $[(L^1)_2Cu(H_2O)(phen)](NO_3)$.

We devised a convenient methodology to extract information on the Ligand Field orbital scheme (the splitting of the d orbitals in the given environment) handling the date of Time Dependent (TD) DFT calculations. The density difference maps are identifying the d-d transitions as zones showing the specific shapes of the *d*-type orbitals (see the right side of Figure V.2). In this representation, the blue areas display the zones where the electron arrives, after transition, while the yellow one, the effective orbitals from where it was released. In all the TD transitions of this system the blue zone is basically the same, corresponding the singly occupied orbital of the

d^9 configuration, its four-lobe shape suggesting the x^2-y^2 function. The yellow shapes and the energy of the related transitions are enabling the identification of the doubly occupied orbitals in the LF split of the d^9 complex. In this way, taking the reverse of the TD energies, as suggested in the middle panel of Figure V.2, corroborated with qualitative information on the involved orbitals, one may identify the LF diagram sketched in the left side.

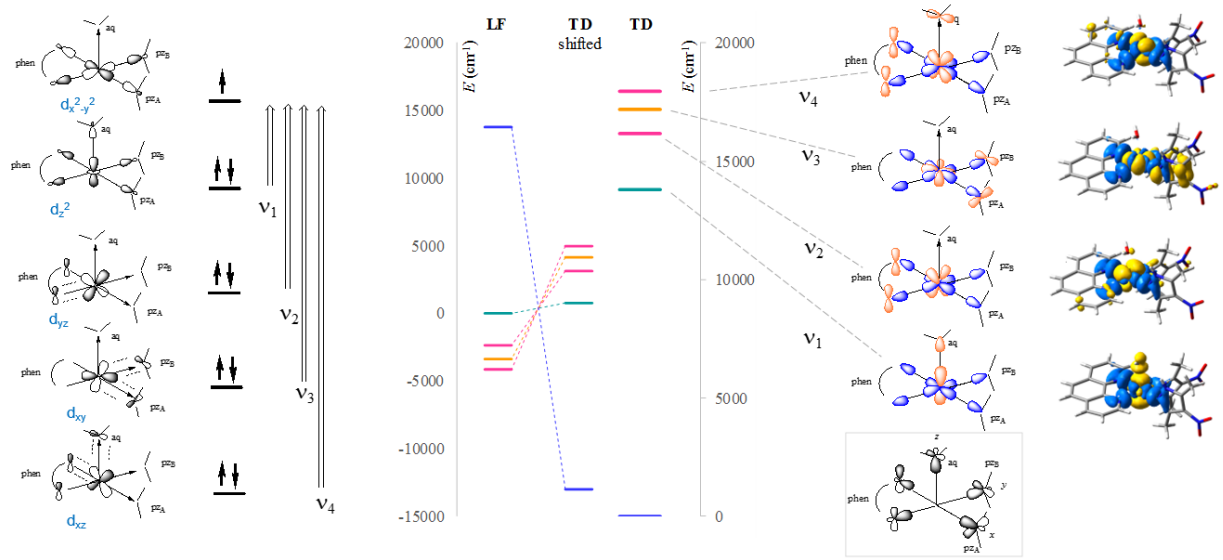

Figure V.2. Ligand Field energy diagram (left panel and the left-side of the central graph) deduced from the computed TD energies (the right-side of the central graph) and the schematized TD density difference maps (right-side panel). The computed TD difference maps, in miniature, are on the right side, with blue denoting density accumulation and yellow, density depletion.

With the LF diagram known, one may nicely correlate the computed (and experimental) UV-VIS spectrum with the Landé factors of the system:

$$g_x = g_0 + \frac{2\lambda}{\Delta_{xz\rightarrow x^2-y^2}}, \qquad \text{(IV.1.a)}$$

$$g_y = g_0 + \frac{2\lambda}{\Delta_{yz\rightarrow x^2-y^2}}, \qquad \text{(IV.1.b)}$$

$$g_z = g_0 + \frac{8\lambda}{\Delta_{xy\rightarrow x^2-y^2}}, \qquad \text{(IV.1.c)}$$

where g_0 = 2.0023, $\Delta_{xz\rightarrow x^2-y^2} \approx \nu_4$ = 17957.2 cm^{-1}, $\Delta_{yz\rightarrow x^2-y^2} \approx \nu_2$ = 16156.4 cm^{-1} and $\Delta_{xy\rightarrow x^2-y^2} \approx \nu_3$ = 17184.5 cm^{-1}. With the spin-orbit fitted at λ = 540.9 cm^{-1}, one obtains g_x = 2.062, g_y = 2.069 and g_z = 2.254, i.e. a good correlation with the experimental values (listed in the body of Fig. V.1). Note that TD-DFT is particularly suited to the account of the d^9 LF spectra, because both sides are implying one-particle transitions. In general, it may not work well for other LF cases (e.g. d^7 or d^8 complexes) that include also two-electron processes.

V.b. Spin coupling in Mn(III) complexes: ferromagnetic *vs.* antiferromagnetic coupling

The magneto-structural considerations on transition metal coordination compounds continues with a series of new manganese (III) complexes [50]. More concretely, there are three systems, with the following formulas and labels: $[Mn_2(5MeO\text{-}salen)_2(RCOO)]X$, $R=CH_3^-$, $X=ClO_4^-$ (**Mn1**), PF_6^- (**Mn2**), $CF_3SO_3^-$ (**Mn3**). These consist in binuclear units based on salen-type ligands (where salen is N,N'-bis(salicyliden)-ethylenediamine), further bridged in 1D chains by *syn-anti* carboxylate ions.

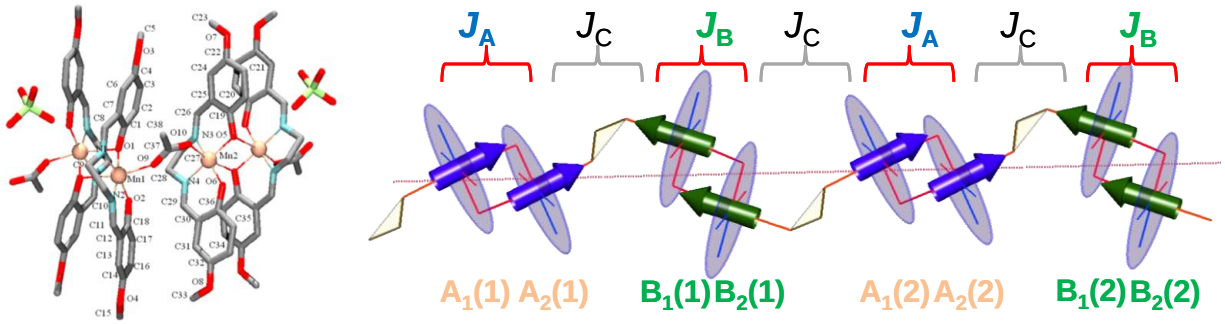

Figure V.3. Unitary molecular sequence of compound **Mn1** and the scheme for the magnetic anisotropy and spin coupling in the chains of isostructural **Mn1-Mn3** compounds.

The characteristic feature of these systems is the interplay between the local anisotropy on the Mn(III) centres, expressed by relatively large ZFS parameters and the exchange coupling, along the chain. The Fig.V.3 illustrates the molecular unit of compound **Mn1** and sketches the magnetic interactions along a chain sequence. The $D<0$ parameters (e.g. for Mn1, fitted= -5.15 cm^{-1}, computed=-3.27 cm^{-1}) are determining a net magnetization axis, perpendicular on the mean plane of the salen-type ligands, suggested by arrows in the rigth side of the Fig.V3. The alternation of the arrows in this scheme suggests also the ferromagnetic coupling ($J>0$) inside the dimeric units and antiferromagnetic ($J<0$) between them (i.e. across the carboxylate bridges). This assignment is supported by calculations, found in semiquantitative agreement with the fit to the experimental data (magnetic susceptibility and magnetization curves at different temperatures). In more detail, the dimeric units belong to two crystallographic classes denoted by A and B, which, in fact, are quite similar as geometry and magnetic parameters. The ferromagnetic coupling is interpreted as due to an accidental orthogonality within dimeric units, while the antiferromagnetic situation is determined by the orbital overlap induced by the low local symmetry on the carboxylate bridges.

Conclusions

The breakthroughs of our work can be summarized as follows:

♦ Concerning the problem of the exchange and dipolar interactions in TEMPO dimers, we contributed with new magneto-structural correlations.

♦ Related to the hyperfine interactions, we projected new Slater-type basis, adjusted for EPR purposes.

♦ We have developed a method for extrapolating the formation energy of the supramolecular (host-guest) complexes based on increasing precision plane-waves calculations.

♦ In the albumin-gold nanoparticles systems, we extracted important information about the dynamics of the formation of the nanoparticles and the related changes of the protein.

♦ We realised the extension of a model which correlates the averaged distances in a biradicals series with the shapes of EPR spectra.

♦ In systems with unstable aromatic radicals (triangulene-type), we proposed the calibration of the coupling parameters, *J*, from CASSCF calculations on small molecules, using then the Heisenberg spin Hamiltonian to approach the upper members of the class.

♦ In coordination systems, we have made an interesting correlation between UV-VIS and EPR spectra of mononuclear copper(II) complexes, via TD-DFT calculations and Ligand Field Models. In coordination polymers of Mn(III) we investigated the interplay between the local magnetic anisotropy and inter-centre exchange coupling.

*
**
***
****

References

[1] M. V. Putz, F. Cimpoesu, M. Ferbinteanu, *Structural Chemistry, Principles, Methods, and Case Studies*. Springer: Cham, 170-186, **2018**.
[2] A. Abragam, B. Bleaney, *Electron Paramagnetic Resonance*. Clarendon Press: Oxford, **1970**.
[3] A. Bencini, D. Gatteschi, *EPR of Exchange Coupled Systems*. Springer-Verlag: Berlin, **1990**.
[4] O. Kahn, *Molecular Magnetism*, Wiley-VCH: Weinheim, **1993**.
[5] a) E. Coronado, P. Delhaès, D. Gatteschi, J. S. Miller, *Molecular Magnetism: From Molecular Assemblies to the Devices*, Springer: Heidelberg, **1996** b) J. S. Miller, M. Drillon, (eds), *Magnetism: Molecules to Materials*. Wiley-VCH: Weinheim, **2001**.
[6] a) F. Troiani, M. Affronte, Molecular spins for quantum information technologies. *Chem. Soc. Rev.* **2011**, *40*, 3119-3129; b) L. Bogani, W. Wernsdorfer, Molecular spintronics using single-molecule magnets. *Nature Mat.* **2008**, *7*, 179-186.
[7] G. Ionita, A. M. Ariciu, I. M. Turcu, V. Chechik, Properties of polyethylene glycol/cyclodextrin hydrogels revealed by spin probes and spin labelling methods. *Soft Matter* **2014**, *10*, 1778–1783.
[8] G. Ionita, A. M. Ariciu, D. K. Smith, V. Chechik, Ion exchange in alginate gels – dynamic behaviour revealed by electron paramagnetic resonance. *Soft Matter* **2015**, *11*, 8968-8974.
[9] G. Ionita, V. Chechik, Exploring polyethylene glycol/cyclodextrin hydrogels with spin probes and EPR spectroscopy. *Chem. Commun.* **2010**, *46*, 8255–8257.
[10] Y. Pontillon, A. Grand, T. Ishida, E. Lelievre-Berna, T. Nogami, E. Ressouche, J. Schweizer, Spin density of a ferromagnetic TEMPO derivative: polarized neutron investigation and ab initio calculation. *J. Mater. Chem.* **2000**, *10*, 1539-1546.
[11] a) W. Duffy Jr., J. F. Dubach, P. A. Pianetta, J. F. Deck, D. L. Strandburg, A. R. Miedena, Antiferromagnetic Linear Chains in the Crystalline Free Radical BDPA. *J. Chem. Phys.* **1972,** *56*, 2555-2561; b) I. Watanabe, N. Wada, H. Yano, T. Okuno, K. Awaga, S. Ohira, K. Nishiyama, K. Nagamine, Muon-spin-relaxation study of the ground state of the two-dimensional S=1 kagoméantiferromagnet [2-(3-N-methyl-pyridium)-4,4,5,5-tetramethyl-4,5-dihydro-1H-imidazol-1-oxyl 3-N-oxide]BF4, *Phys. Rev. B* **1998,** *58*, 2438-2441; c) T. Ishida, S. Ohira, T. Ise, K. Nakayama, I. Watanabe, T. Nogami, K. Nagamine, Zero-field muon spin rotation study on genuine organic ferromagnets, 4-arylmethyleneamino-2,2,6,6-tetramethylpiperidin-1-yloxyls (aryl=4-biphenylyl and phenyl). *Chem. Phys. Lett.* **2000**, *330*, 110-117.
[12] a) R. Chiarelli, M. A. Novak, A. Rassat, J. L. Tholence, A ferromagnetic transition at 1.48 K in an organic nitroxide. *Nature* **1993**, *363*, 147–149; b) M. Takahashi, P. Turek, Y. Nakazawa, M. Tamura, K. Nozawa, D. Shiomi, M. Ishikawa, M. Kinoshita, Discovery of a quasi-1D organic ferromagnet, p-NPNN. *Phys. Rev. Lett.* **1991**, *67*, 746-748.
[13] a) C. Aoki, T. Ishida, T. Nogami, Molecular Metamagnet [Ni(4ImNNH)2(NO3)2] (4ImNNH = 4-Imidazolyl Nitronyl Nitroxide) and the Related Compounds Showing Supramolecular H-Bonding Interactions. *Inorg. Chem.* **2003**, *42*, 7616-7625; b) R. G. Hicks, M. T. Lemaire, L. Ohrstrom, J. F. Richardson, L. K. Thompson, Z. Q. Xu, Strong Supramolecular-Based Magnetic Exchange in π-Stacked Radicals. Structure and Magnetism of a Hydrogen-Bonded Verdazyl Radical:Hydroquinone Molecular Solid. *J. Am Chem Soc.* **2001**, *123*, 7154-7159; c) D. Papoutsakis, J. B. Kirby, J. E. Jackson, D. G. Nocera, From Molecules to the Crystalline Solid: Secondary Hydrogen-Bonding Interactions of Salt Bridges and Their Role in Magnetic Exchange. *Chem. Eur. J.* **1999**, *5*, 1474-1480.
[14] a) A. Caneschi, D. Gatteschi, P. Rey, Structure and magnetic ordering of a ferrimagnetic helix formed by manganese(II) and a nitronyl nitroxide radical. *Inorg. Chem.* **1991**, *30*, 3936-3941; b) H. Iwamura, K. Inoue, N. Koga, T. Hayamizu, *Magnetism: A Supramolecular Function* (Eds.: O. Kahn), Kluwer: Dordrecht, The Netherlands, **1996**, pp. 157; c) O. Kahn, Chemistry and Physics of Supramolecular Magnetic Materials. *Acc. Chem. Res.* **2000**, *33*, 647-657.
[15] M. Abe, Diradicals. *Chem. Rev.* **2013**, *113(9)*, 7011–7088.
[16] W. Koch, M.C. Holthausen, *A Chemist's Guide to Density Functional Theory*, VCH: Berlin, **2001**.
[17] L. Noodleman, Valence bond description of antiferromagnetic coupling in transition metal dimers. *J. Chem. Phys.* **1981**, *74*, 5737–5743.
[18] A. Bencini, F. Totti, C. A. Daul, K. Doclo, P. Fantucci, V. Barone, Density Functional Calculations of Magnetic Exchange Interactions in Polynuclear Transition Metal Complexes. *Inorg. Chem.* **1997**, *36*, 5022–5030.
[19] a) C. Adamo, D. Jacquemin, The calculations of excited-state properties with Time-Dependent Density Functional Theory. *Chem. Soc. Rev.* **2013**, *42*, 845-856; b) A. D. Laurent, C. Adamo, D. Jacquemin, Dye chemistry with time-dependent density functional theory. *Phys. Chem. Chem. Phys.* **2014**, *16*, 14334-14356.
[20] J. B. Foresman, Æ. Frisch, *Exploring Chemistry with Electronic Structure Methods* (3rd ed). Gaussian, Inc.: Wallingford, CT, **2015**.
[21] S. Shaik, P. C. Hiberty, *A chemist's guide to valence bond theory*. John Wiley & Sons, Inc, Hoboken, New Jersey, **2007**.
[22] M. C. Buta, A. M. Toader, B. Frecus, C. I. Oprea, F. Cimpoesu, G. Ionita, Molecular and Supramolecular Interactions in Systems with Nitroxide-based Radicals. *Int. J. Mol. Sci.* **2019**, *20*, 4733.

[23] M. Mitani, H. Mori, Y. Takano, D. Yamaki, Y. Yoshioka, K. Yamaguchi, Density functional study of intramolecular ferromagnetic interaction through m-phenylene coupling unit (I): UBLYP, UB3LYP and UHF calculation. *J. Chem. Phys.* **2000**, *113*, 4035–4050.
[24] T. Onishi, Y. Takano, Y. Kitagawa, T. Kawakami, Y. Yoshioka, K. Yamaguchi, Theoretical study of the magnetic interaction for M–O–M type metal oxides. Comparison of broken-symmetry approaches. *Polyhedron* **2001**, *20*, 1177–1184.
[25] M. J. Frisch, G. W. Trucks, H. B. Schlegel, G. E. Scuseria, M. A. Robb, J. R. Cheeseman, G. Scalmani, V. Barone, G. A. Petersson, H. Nakatsuji, X. Li, M. Caricato, A. Marenich, J. Bloino, B. G. Janesko, R. Gomperts, B. Mennucci, H. P. Hratchian, J. V. Ortiz, A. F. Izmaylov, J. L. Sonnenberg, D. Williams-Young, F. Ding, F. Lipparini, F. Egidi, J. Goings, B. Peng, A. Petrone, T. Henderson, D. Ranasinghe, V. G. Zakrzewski, J. Gao, N. Rega, G. Zheng, W. Liang, M. Hada, M. Ehara, K. Toyota, R. Fukuda, J. Hasegawa, M. Ishida, T. Nakajima, Y. Honda, O. Kitao, H. Nakai, T. Vreven, K. Throssell, J. A. Montgomery, Jr., J. E. Peralta, F. Ogliaro, M. Bearpark, J. J. Heyd, E. Brothers, K. N. Kudin, V. N. Staroverov, T. Keith, R. Kobayashi, J. Normand, K. Raghavachari, A. Rendell, J. C. Burant, S. S. Iyengar, J. Tomasi, M. Cossi, J. M. Millam, M. Klene, C. Adamo, R. Cammi, J. W. Ochterski, R. L. Martin, K. Morokuma, O. Farkas, J. B. Foresman, and D. J. Fox, *Gaussian 09*, Revision A.02. Gaussian, Inc., Wallingford CT, **2016**.
[26] I. Matei, C. M. Buta, I. M. Turcu, D. Culita, C. Munteanu, G. Ionita, Formation and Stabilization of Gold Nanoparticles in Bovine Serum Albumin Solution. *Molecules* **2019**, *24*, 3395.
[27] D. V. Sotnikov, A. N. Berlina, V. S. Ivanov, A. V. Zherdev, B. B. Dzantiev, Adsorption of proteins on gold nanoparticles: One or more layers? *Coll. Surf. B* **2019**, *173*, 557–563.
[28] S. Dominguez-Medina, S. McDonough, P. Swanglap, C. F. Landes, S. Link, In situ measurement of bovine serum albumin interaction with gold nanospheres. *Langmuir* **2012**, *28*, 9131−9139.
[29] R. Khandelia, A. Jaiswal, S. S. Ghosh, A. Chattopadhyay, Gold nanoparticle–protein agglomerates as versatile nanocarriers for drug delivery. *Small* **2013**, *9*, 3494–3505.
[30] J. Turkevich, P. C. Stevenson, J. A. Hillier, Study of the nucleation and growth processes in the synthesis of colloidal gold. Discuss. *Faraday Soc.* **1951**, *11*, 55–59.
[31] S. H. Brewer, W. R. Glomm, M. C. Johnson, M. K. Knag, S. Franzen, Probing BSA binding to citrate-coated gold nanoparticles and surfaces. *Langmuir* **2005**, *21*, 9303–9307.
[32] P. Khullar, V. Singh, A. Mahal, P. N. Dave, S. Thakur, G. Kaur, J. Singh, S. S. Kamboj, M. S. Bakshi, Bovine serum albumin bioconjugated gold nanoparticles: Synthesis, Hemolysis, and cytotoxicity toward cancer cell lines. *J. Phys. Chem. C* **2012**, *116*, 8834−8843.
[33] J. Xie, J. Y. Lee, D. I. C. Wang, Synthesis of single-crystalline gold nanoplates in aqueous solutions through biomineralization by serum albumin protein, *J. Phys. Chem. C* **2007**, *111*, 10226–10232.
[34] N. Basu, R. Bhattacharya, P. Mukherjee, Protein-mediated autoreduction of gold salts to gold nanoparticles, *Biomed. Mater.* **2008**, *3*, 034105.
[35] M. T. Căproiu, G. Ioniță, C. Drăghici, P. Ioniță, Synthesis and characterisation of several di-, tri-, and tetra-radicals linked by flexible or rigidlinkers. *Arkivoc* **2008**, *xiv*, 158-165.
[36] W. L. Jorgensen, D. S. Maxwell, J. Tirado-Rives, Development and testing of the OPLS all-atom force field on conformational energetics and properties of organic liquids. *J. Am. Chem. Soc.* **1996**, *118 (45)*, 11225–11236.
[37] J. A. Rackers, M. L. Laury, C. Lu, Z. Wang, L. Lagardère, J.-P. Piquemal, P. Ren, J. W. Ponder, TINKER 8: A Modular Software Package for Molecular Design and Simulation. *J. Chem. Theory Comp.* **2018**, *14*, 5273-5289.
[38] A. M. Toader, C. M. Buta, B. Frecus, A. Mischie, F. Cimpoesu, Valence Bond Account of Triangular Polyaromatic Hydrocarbons with Spin: Combining Ab Initio and Phenomenological Approaches. *J. Phys. Chem. C* **2019,** *123*, 6869-6880.
[39] F. Cimpoesu, C. Buta, M. Ferbinteanu, M. R. Philpott, A. Stroppa, M. V. Putz, Electronic Structure of Linear Polyacenes. *Curr. Org. Chem.* **2017**, *21*, 1-8.
[40] K. S. Novoselov, A. K. Geim, S. V. Morozov, D. Jiang, Y. Zhang, S. V. Dubonos, I. V. Grigorieva, A. A. Firsov, Electric Field Effect in Atomically Thin Carbon Films. *Science* **2004**, *306*, 666-669.
[41] M. J. Allen, V. C. Tung, R. B. Kaner, Honeycomb Carbon: A Review of Graphene. *Chem. Rev.* **2010**, *110*, 132-145.
[42] A. A. Ovchinnikov, Multiplicity of the Ground State of Large Alternant Organic Molecules with Conjugated Bonds. *Theor. Chem. Acc.* **1978**, *47*, 297-304.
[43] A. Rajca, S. Rajca, S. R. Desai, Macrocyclic. pi.-Conjugated Carbopolyanions and Polyradicals Based upon Calix [4] arene and Calix [3] arene Rings. *J. Am. Chem. Soc.* **1995**, *117*, 806.
[44] E. Clar, D. G. Stewart, Aromatic Hydrocarbons. LXV. Triangulene Derivatives. *J. Am. Chem. Soc.* **1953**, *75*, 2667-2672.
[45] L. Beer, S. K. Mandal, R. W. Reed, R. T. Oakley, F. S. Tham, B. Donnadieu, R. C. Haddon, The first Electronically Stabilized Phenalenyl Radical: Effect of Substituents on Solution Chemistry and Solid-state Structure. *Cryst. Growth Des.* **2007**, *7*, 802–809.
[46] Y. Morita, S. Suzuki, K. Sato, T. Takui, Synthetic Organic Spin Chemistry for Structurally Well-defined Open-shell Graphene Fragments. *Nature Chem.* **2011**, *3*, 197-204.

[47] N. Pavliček, A. Mistry, Z. Majzik, N. Moll, G. Meyer, D. J. Fox, L. Gross, Synthesis and Characterization of Triangulene. *Nat. Nanotech.* **2017**, *12*, 308–311.
[48] C. M. Buta, M. M. Radu, A. Mischie, Ch. M. Zalaru, G. Ionita, M. Ferbinteanu, Experimental and computational characterization of structural and spectroscopic features of mixed ligand copper complexes-prototypes for square-pyramidal stereochemistry. *Polyhedron* **2019,** *170*, 771–782**.**
[49] R. Hüttel, O. Schäfer, P. Jochum, Die Jodierung der Pyrazole. *Liebigs Ann. Chem*. **1955**, *593*, 200-207.
[50] F. Cimpoesu, T. Spataru, C. M. Buta, H. Borrmann, O. G. Moga, M. Ferbinteanu, Spin Coupling and Magnetic Anisotropy in 1D Complexes with Manganese(III) Units and Carboxylate Bridges. Synthesis and Analysis, Calculations and Models. *Eur. J. Inorg. Chem.* **2018,** *12*, 1409–1418.

List of works and participation in scientific events

List of scientific works for the PhD thesis

1. F. Cimpoesu, T. Spataru, C. M. Buta, H. Borrmann, O. G. Moga, M. Ferbinteanu, Spin Coupling and Magnetic Anisotropy in 1D Complexes with Manganese(III) Units and Carboxylate Bridges. Synthesis and Analysis, Calculations and Models. *European Journal of Inorganic Chemistry* **2018**, *12*, 1409–1418. (F.I. = 2,578)

2. A. M. Toader, C. M. Buta, B. Frecus, A. Mischie, F. Cimpoesu, Valence Bond Account of Triangular Polyaromatic Hydrocarbons with Spin: Combining Ab Initio and Phenomenological Approaches. *The Journal of Physical Chemistry C* **2019**, *123*, 6869-6880. (F.I. = 4,309)

3. M. C. Buta, A. M. Toader, B. Frecus, C. I. Oprea, F. Cimpoesu, G. Ionita, Molecular and Supramolecular Interactions in Systems with Nitroxide-based Radicals. *International Journal of Molecular Sciences* **2019**, *20*, 4733. (F.I. = 4,183)

4. C. M. Buta, M. M. Radu, A. Mischie, Ch. M. Zalaru, G. Ionita, M. Ferbinteanu, Experimental and computational characterization of structural and spectroscopic features of mixed ligand copper complexes-prototypes for square-pyramidal stereochemistry. *Polyhedron* **2019**, *170*, 771–782. (F.I. = 2,067)

5. I. Matei, C. M. Buta, I. M. Turcu, D. Culita, C. Munteanu, G. Ionita, Formation and Stabilization of Gold Nanoparticles in Bovine Serum Albumin Solution. *Molecules* **2019**, *24*, 3395. (F.I. = 3,060)

List of scientific works concerning other projects

6. F. Cimpoesu, C. Buta, M. Ferbinteanu, M. R. Philpott, A. Stroppa, M. V. Putz, Electronic Structure of Linear Polyacenes. *Current Organic Chemistry* **2018**, *21(27)*, 2768 - 2775.

7. B. Frecus, C. M. Buta, C. I. Oprea, A. Stroppa, M. V. Putz, F. Cimpoesu, Noble gas endohedral fullerenes, $Ng@C_{60}$ (Ng=Ar, Kr): a particular benchmark for assessing the account of non.covalent interactions by density functional theory calculations. *Theoretical Chemistry Accounts* **2016**, *135*, 133.

8. A. M. Toader, M. C. Buta, D. Maftei, M. V. Putz, F. Cimpoesu, Atoms in Generalized Orbital Configurations: Towards Atom-Dedicated Density Functionals. *International Journal of Molecular Sciences* **2019**, *20*, 5943.

9. M. Ferbinteanu, C. Buta, A. M. Toader, F. Cimpoesu, cap. The Spin Coupling in the Polyaromatic Hydrocarbons and Carbon-based Materials în *Carbon-related Materials-in*

Recognition of Nobel Lectures by Prof. Akira Suzuki in ICCE (Ed. S. Kaneko, P. Mele, T. Endo). Springer Verlag: Cham, pp 327-371, **2017**.

Scientific manifestations participation

1. Maria Cristina Buta, Ana Maria Toader, Gabriela Ioniță, Structural Analyses of Interacting Nitroxide-based Organic Radicals, Nano-Modeling of Strategic Materials for Knowledge Economy (NANO-MOD), 16-17 mai 2018, Timișoara, România.

2. Maria Cristina Buta, Ana Maria Toader, Corneliu I. Oprea, Gabriela Ioniță, Fănică Cimpoeșu, Magneto-structural Correlations with Nitroxide Radicals, 18th International Balkan Workshop on Applied Physics (IBWAP), 10-13 iulie 2018, Constanța, România.

3. Maria Cristina Buta, Ana Maria Toader, Fănică Cimpoeșu, Modeling the Long-range Coupling in Spin-probe Systems, 4th International Conference on Analytical Chemistry (RO-ICAC), 1-3 septembrie 2018, București, România.

4. Maria Cristina Buta, Ana Maria Toader, Gabriela Ioniță, Through-space and Through-solvent Interactions between Nitroxide-based Stable Radicals, 28-30 octombrie 2018, Cluj-Napoca, România.

5. Ana Maria Toader, Maria Cristina Buta, Bogdan Frecuș, Alice Mischie, Fănică Cimpoeșu, Triangular Polyaromatic Hydrocarbons with Spin, Nano-Modeling of Strategic Materials for Knowledge Economy (NANO-MOD), 22-23 aprilie 2019, Timișoara, România.

6. Maria Cristina Buta, Alice Mischie, Gabriela Ioniță, Marilena Ferbințeanu, The Modeling of Square-pyramidal Mixed Ligand Copper Complexes, Nano-Modeling of Strategic Materials for Knowledge Economy (NANO-MOD), 22-23 aprilie 2019, Timișoara, România.

7. Ana Maria Toader, Maria Cristina Buta, Bogdan Frecuș, Alice Mischie, Fănică Cimpoeșu, Triangular Polyaromatic Hydrocarbons with Spin, 19th International Balkan Workshop on Applied Physics (IBWAP), 16-19 iulie 2019, Constanța, România

Projects participation list

1. Methodological advances and theoretical experiments on the bonding regime and properties design. From atoms to supra-molecules. PN-II-ID-PCE-2012-4-0633, project director Dr. Fănică Cimpoeșu.

2. Critical analyses and fundamental theoretical developments in computational chemistry (CRAFT), PN-III-P4-ID-PCE-2016-0689, project director Dr. Fănică Cimpoeșu.